Continuous catchment-scale monitoring of geomorphic processes with a 2-D seismological array

Continuous catchment-scale monitoring of geomorphic processes with a 2-D seismological array

Arnaud Burtin,[1] Niels Hovius,[1] David T. Milodowski,[2] Yue-Gau Chen,[3] Yih-Min Wu,[3] Ching-Weei Lin,[4] Hongey Chen,[3] Robert Emberson,[1] and Peih-Lin Leu[5]

Received 26 September 2012; revised 30 July 2013; accepted 22 August 2013; published 19 September 2013.

[1] Distributed activity of geomorphic processes with different spatiotemporal scales is hard to monitor in detail with conventional methods but might be detected with seismometers. From July to September 2010, we deployed 14 seismometers to evaluate the ability of a two-dimensional array with small interstation distances (11 km) to continuously monitor geomorphic processes in a mountain catchment (370 km^2) in Taiwan. Spectral analysis of seismic records highlights different sources with high-frequency content (>1 Hz), consistent with hillslope and river processes. Using a common detection algorithm and a location technique based on the timing of seismic amplitude, we have located 314 near-surface events, most of which (69%) occurred during daily convective storms. Event activity was positively correlated with the precipitation intensity, but this relation was not uniform in the catchment. High-resolution satellite images and air photos did not show geomorphic change during the study, which did not have any episodes of extreme precipitation. A majority of events (61%) were collocated with preexisting geomorphic features (landslide scars, gullies) within the uncertainty on location (9% of interstation distance). The combination of event location and timing suggests a geomorphic source of recorded signals and most events had the seismic characteristics of rockfall, debris avalanches, or slides. Reactivation of prior erosion sites by such processes is difficult to detect with imagery, but can possibly be resolved by seismic monitoring. When proven, this approach will allow a spatially comprehensive survey of geomorphic activity at the catchment scale, with temporal detail sufficient to evaluate the exact (meteorological) conditions under which process events occur.

Citation: Burtin, A., N. Hovius, D. T. Milodowski, Y.-G. Chen, Y.-M. Wu, C.-W. Lin, H. Chen, R. Emberson, and P.-L. Leu (2013), Continuous catchment-scale monitoring of geomorphic processes with a 2-D seismological array, *J. Geophys. Res. Earth Surf.*, *118*, 1956–1974, doi:10.1002/jgrf.20137.

1. Introduction

[2] Geomorphic processes as diverse as rockfall, landsliding, debris flow, and fluvial sediment transport occur distributed across landscapes under a range of external conditions. Their individual rates and interactions together determine the sediment flux from a landscape, the sensitivity and response of that landscape to changes in external forcing, and the hazard risk associated with erosion. To understand the mechanisms of geomorphic processes and their connectedness, and ultimately the dynamics of erosional landscapes, it is necessary to know what process events happen where in a landscape, how much material is involved, and when they occur with a time and space resolution that permits direct comparison with records of external forcing. Established monitoring techniques and approaches meet these requirements only to a degree. Optical remote sensing using satellite data or aerial photography is a common basis for mapping of erosional change over large areas with meter-scale spatial resolution [e.g., *Guzzetti et al.*, 2000; *Chang et al.*, 2006]. However, this approach commonly yields constraints on erosion areas rather than volumes, and its time resolution is set by the frequency of the data acquisition. This resolution is of the order of a week at best, and data availability is highly dependent upon atmospheric conditions, affecting the efficiency of detection especially during periods of precipitation when geomorphic activity is most likely. At this time resolution, it is difficult to link geomorphic change by rapid processes to the specific conditions from which they resulted. Moreover, optical detection techniques crucially rely on changes in the reflective properties of the imaged surface [e.g., *Lin et al.*, 2011], commonly associated with removal of vegetation or soil cover, precluding reliable observation of areas with recurring

Additional supporting information may be found in the online version of this article.

[1]GeoForschungsZentrum, Helmholtz Centre Potsdam, Potsdam, Germany.
[2]School of Geosciences, University of Edinburgh, Edinburgh, UK.
[3]Department of Geosciences, National Taiwan University, Taipei, Taiwan.
[4]Department of Earth Sciences, National Cheng-Kung University, Taipei, Taiwan.
[5]Seismological Center, Central Weather Bureau, Taipei, Taiwan.

Corresponding author: A. Burtin, GeoForschungsZentrum, Helmholtz Centre Potsdam, Telegrafenberg, Potsdam DE-14473, Germany. (burtin@gfz-potsdam.de)

2169-9003/13/10.1002/jgrf.20137

geomorphic activity [*Reid*, 1998; *Brardinoni et al*., 2003]. In situ monitoring techniques do not suffer from these restrictions. Using wire and pressure sensors, radar, laser, or video, these techniques have been developed for site-specific, continuous monitoring of mass wasting and channel flow, often for early warning purposes [*Itakura et al*., 2005; *Arattano and Marchi*, 2008]. This approach can yield data with very high temporal resolution, allowing assessment of the specific conditions under which an event occurred. However, monitoring equipment is often set up in places with a high likelihood of activity, which introduces a bias to observations, whilst the approach also lacks a view on the landscape at large. Thus, these two approaches tend to offer spatial or temporal resolution, but not both.

[3] Acoustic waves or ground vibrations induced by the impact of moving sediment particles on their substrate have been exploited for in situ or focused geomorphic monitoring [*Huang et al*., 2007; *Barton et al*., 2010]. They can be registered by geophones installed along a channel or at a check dam [*Hsiao et al*., 2007] and are used in early warning systems in mountain catchments [*Berti et al*., 2000; *Badoux et al*., 2009]. However, acoustic monitoring is limited to the survey of single-channel sections and does not allow the systematic characterization of erosion in a larger area. Following a similar principle, seismic sensors (seismometers and accelerometers) are increasingly employed in the monitoring of hillslopes [*Burtin et al*., 2009; *Helmstetter and Garambois*, 2010] and river processes [*Burtin et al*., 2010, 2011; *Hsu et al*., 2011]. The interest of seismometers is in their ability to continuously record ground vibrations from distributed sources. The potential of seismic monitoring has been explored in various geomorphic contexts, including bed load transport [e.g., *Burtin et al*., 2011; *Tsai et al*., 2012], landslides [e.g., *Suriñach et al*., 2005], debris flows [e.g., *Marchi et al*., 2002; *Burtin et al*., 2009], snow avalanches [e.g., *St. Lawrence and Williams*, 1976; *Leprettre et al*., 1998; *Lacroix et al*., 2012], rockfalls [e.g., *Deparis et al*., 2008, *Helmstetter and Garambois*, 2010], rock avalanches [e.g., *Dammeier et al*., 2011], and sea cliff erosion [e.g., *Adams et al*., 2005]. In addition to these observational applications, modeling of seismic signals is also relevant to understanding of the physics and dynamics of mass movements [*Brodsky et al*., 2003; *Favreau et al*., 2010]. There is now a body of work that clearly demonstrates the utility of seismological approaches to monitoring of surface processes. However, most of this work has been restricted to individual processes, specific events, and/or single sites. Since seismic waves caused by geomorphic processes can travel over large distances [e.g., *Ekström and Stark*, 2013], seismology also has potential geomorphological applications on larger scales. This could offer a useful combination of spatial coverage and temporal resolution for landscape-scale monitoring of geomorphic activity, provided that there is a favorable trade-off between the size and the spatial resolution of the seismic instrument network, and a sufficient ability to detect, identify, and locate multiple, distributed events of a variety of processes.

[4] The geometry of a seismic array has a primary control on the ability to locate distributed geomorphic events. Analysis of seismic data from the Hi-CLIMB array, a temporary seismological experiment in the Himalayas [*Nábělek et al*., 2009], has demonstrated that a linear instrument alignment is not fully adapted to the location of geomorphic process events that occurred off the array trend [*Burtin et al*., 2009]. Instead, the many directions that exist between seismic stations in a two-dimensional (2-D) array cover a large range of azimuths, reducing drastically the ambiguities in the location of sources [e.g., *Swanson*, 1992]. Two-dimensional arrays can be configured for a specific purpose. For example, an array of sensors installed in concentric rings with a small aperture (10^2 m) allows high-resolution monitoring of process activity within a small area [e.g., *Lacroix and Helmstetter*, 2011] and possibly the tracking of mobile sources [*Lacroix et al*., 2012]. In such a configuration, the spatial coverage is limited to a predefined geomorphic domain such as a hillslope affected by a landslide or an avalanche gully, precluding observation of an entire landscape. Catchment-scale (10^1–10^2 km^2) monitoring of a range of geomorphic processes requires a 2-D array geometry with a larger interstation distance, trading location accuracy for spatial coverage, as well as event detection and location techniques suited to the specifics of geomorphic source signals. This has not been attempted before.

[5] In this study, we explore the use of a dedicated seismic array to monitor surface processes at the scale of a catchment. During summer 2010, we deployed a 2-D array of seismometers in the Chenyoulan catchment (370 km^2) in the western Central Range of Taiwan. Following a description of the seismic experiment and its setting, we introduce the different stages of the analysis of seismic signals, from event detection to location. The results from our seismic monitoring of the Chenyoulan catchment are then compared with available independent data sets to establish whether our seismic observations match remote-sensed constraints on geomorphic activity and to explore the connection between meteorological conditions, like rainfall intensity and location, and seismically detected near-surface activity in the catchment.

2. Setting and Data Acquisition

2.1. Area of Study

[6] The Chenyoulan River drains an area of 370 km^2 straddling the north-south Chenyoulan thrust fault (Figure 1), one of the major active faults of the Taiwan orogen. Rapid and persistent tectonic shortening across the orogen at a rate of ~90 mm/yr [*Sella et al*., 2002] gives rise to intense seismic activity with frequent, moderate magnitude earthquakes at shallow depths in the Central Range and the Western Foothills [e.g., *Sibuet and Hsu*, 2004]. Dipping to the east, the Chenyoulan thrust fault delineates two main geological domains, with Paleogene slates and metasandstones to the east, and Neogene interbedded shales and sandstones to the west. Compressive strength tests reveal that the older rocks in the eastern part of the catchment are more competent than the western geological units whose shale interbeds have limited frictional strength [*Lin et al*., 2008]. These rocks underlie mountain topography culminating at Yushan, 3952 m above sea level (asl). Throughout the catchment, kilometer-high mountain ridges are separated from bedrock river channels by long, straight hillslopes with uniform modal gradients of around 37°.

[7] From May to October, Taiwan is hit by typhoons [e.g., *Galewsky et al*., 2006] that provide the extreme climatic conditions favorable to frequent triggering of hillslope activity. Sustained, high erosion rates on hillslopes [*Dadson et al*., 2003], driven by frequent, intense precipitation (average

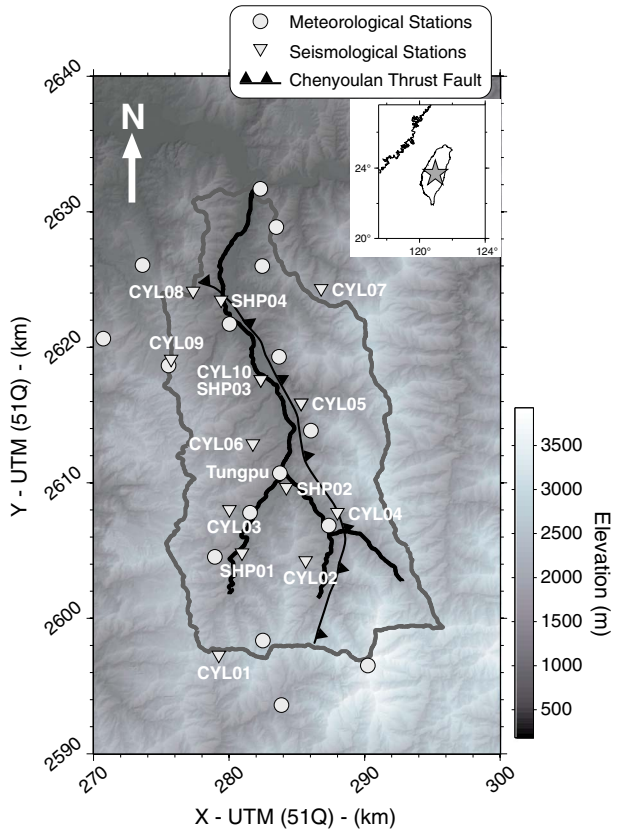

Figure 1. Location and topographic map of the Chenyoulan catchment, Taiwan (gray star on inset map), and array geometry of the instruments deployed from 1 July to 30 September 2010. Seismological and meteorological stations are shown as triangles and circles, respectively. The catchment is delimited by a dark gray line and the main streams are shown by black lines. The Chenyoulan thrust fault, the principal active structure in the catchment, is adapted from *Lin et al*. [2008]. Note the lower density of stations (seismometers and rain gauges) in the eastern part of the catchment due to access limitations.

annual precipitation ~3 m), have caused alluviation of the trunk streams of the catchment. As a result, a gravel braid plain dominates the lower catchment, reaching a width of 300 m at the confluence of the Chenyoulan River with the larger, west flowing Choshui River. In west Taiwan, large earthquakes, $M_w > 7$, such as the M_w 7.6 1999 Chi-Chi earthquake [*Kao and Chen*, 2000], have occurred with regularity [e.g., *Streig et al*., 2007], soliciting a strong geomorphic response [*Meunier et al*., 2007; *Hovius et al*., 2011]. Very high rates of mass wasting after the Chi-Chi earthquake, with more than 48,000 landslides triggered by individual large typhoons between years 1999 and 2006 [*Dadson et al*., 2004; *Lin et al*., 2008; *Hovius et al*., 2011] make the Chenyoulan catchment a suitable location for the development of a seismological technique dedicated to the monitoring of geomorphic activity at the catchment scale. Furthermore, with a relatively limited size, this catchment does not require so many seismometers that logistics could become hard to manage during the experiment in order to resolve relevant geomorphic processes.

2.2. Seismic Data

[8] From 1 July to 30 September 2010, we deployed 14 seismic stations, distributed across the Chenyoulan catchment (Figure 1). Among them, 10 instruments were GURALP CMG-6TD intermediate band sensors (denoted by CYL##) with a flat response in the 0.033–100 Hz frequency band and a preselected sampling rate of 200 samples per second (SPS). These instruments were installed well away from major channels, mostly high in the mountains to record hillslope activity. The remaining four instruments were KINKEI short period sensors (denoted by SHP##) with a natural frequency of 1 Hz. These short-period sensors were located along the main stream at distances of <800 m from the Chenyoulan River in order to monitor river processes (Figure 1). Due to the digitizer specifications of the short period instruments, the sampling rate was limited to 100 SPS. Because we have constrained our analysis below 50 Hz, the difference in sampling rate between the two instrument types has had no effect on data processing.

[9] Site selection criteria for our stations included the absence of persistent, nearby human activity to minimize the signal disturbance by anthropogenic sources, like vehicle traffic and road works. The stations were deployed on flat terrain, at maximum distance to significant breaks in topographic slope to avoid large amplification or attenuation of seismic waves, and with homogeneous substrate suited to manual digging. At each site, we excavated a pit of about 0.6 m deep and installed the seismometer on a level, concrete patch before sealing and covering the instrument. Access restrictions meant that the eastern part of the catchment was less well equipped than the western side. In addition, stations CYL07 and CYL09 were either inaccessible or not operational during most of the survey. Data from these stations have been eliminated from this study. Thus, the average distance between seismometers was 11 ± 6 km (1σ), with closer instrument spacing in the upstream part of the catchment where most geomorphic activity had occurred prior to the survey.

2.3. Meteorological Data

[10] To complement our seismic observations, we have 10 min precipitation rate data recorded at 16 rain gauges in or close to the Chenyoulan catchment (Figure 1; Central Weather Bureau (CWB), Precipitation data, 2010). The seismic survey period was chosen to coincide with the typhoon season, which lasts from May to October [*Chen and Chen*, 2003], and during which most erosion occurs [e.g., *Stark et al*., 2010]. Over our monitoring interval, storm activity was subdued, with a recorded total precipitation of 745 mm at Tungpu in the center of the catchment (Figure 1). One large tropical storm in July (Days 207–209) and a category 3 typhoon, Fanapi, in September (Day 261–262) deposited 185 and 162 mm rainfall, respectively (Figure 2b). This was in marked contrast to the 2009 typhoon season, when up to 3000 mm of rainfall occurred in 4 days during passage of Typhoon Morakot [*Chien and Kuo*, 2011].

2.4. Imagery Data

[11] Satellite imagery and aerial photography necessary to determine a context for the detected surface or near-surface activity and to test the interpretation of seismic data are also available. Erosion features on hillslopes were mapped from

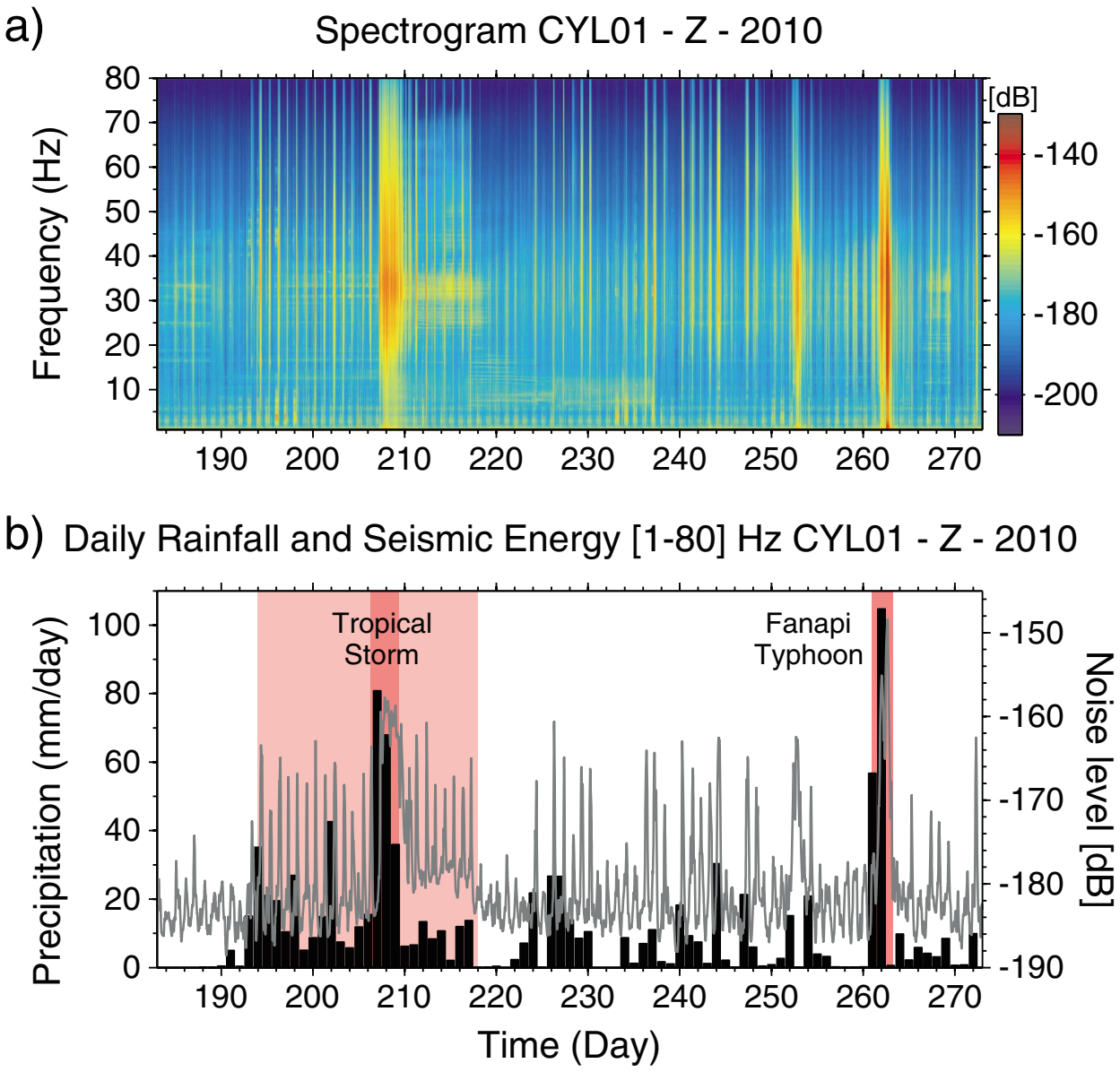

Figure 2. (a) Spectrogram of the vertical continuous seismic signal recorded at CYL01 for the period of experiment. The spectrogram amplitude is given in decibel (dB) relative to the velocity. Blue and red colors stand for low and high seismic energy, respectively. (b) Mean daily rainfall (black) recorded at 16 rain gauges located in and around the Chenyoulan catchment (Figure 1) and average seismic noise level (gray) in the 1–80 Hz frequency band at CYL01 for the same time period. Bursts of high-frequency seismic energy correspond with periods of large precipitation rates. The daily fluctuation of seismic noise (most pronounced during the interval marked in light red) is coherent with the occurrence of local convective storms. The intervals marked in dark red delineate the two main rainfall episodes of the experiment, a tropical storm and a typhoon, Fanapi.

FORMOSAT-2 multispectral (visible to near-infrared) images with a resolution of 8 m. This was done with a classification procedure outlined by *Lin et al*. [2011], applied to images with less than 6% cloud cover, acquired on Days 222, 254, 266, 275, and 285 (from August to October 2010). Briefly, on the FORMOSAT-2 multispectral images, eroded areas are discernable through absence of vegetation. Using a Normalized Difference Vegetation Index (NDVI) criterion [*Lin et al*., 2011], bare land features can be isolated. Bare land with steepness of less than 10°, as well as steep land features smaller than nine adjacent grid cells (576 m^2) were automatically removed from the catalogue. Subsequently, areas of agriculture and construction were removed manually. This procedure identifies erosion areas with an overall accuracy of >95% [*Lin et al*., 2011]. By differencing of erosion maps from successive FORMOSAT-2 images, erosional change can be detected at the scale of individual image pixels (64 m^2) or larger areas. Using 2 m resolution, panchromatic versions of the FORMOSAT-2 images, the results from the NDVI procedure were checked manually to validate the quality of the analysis

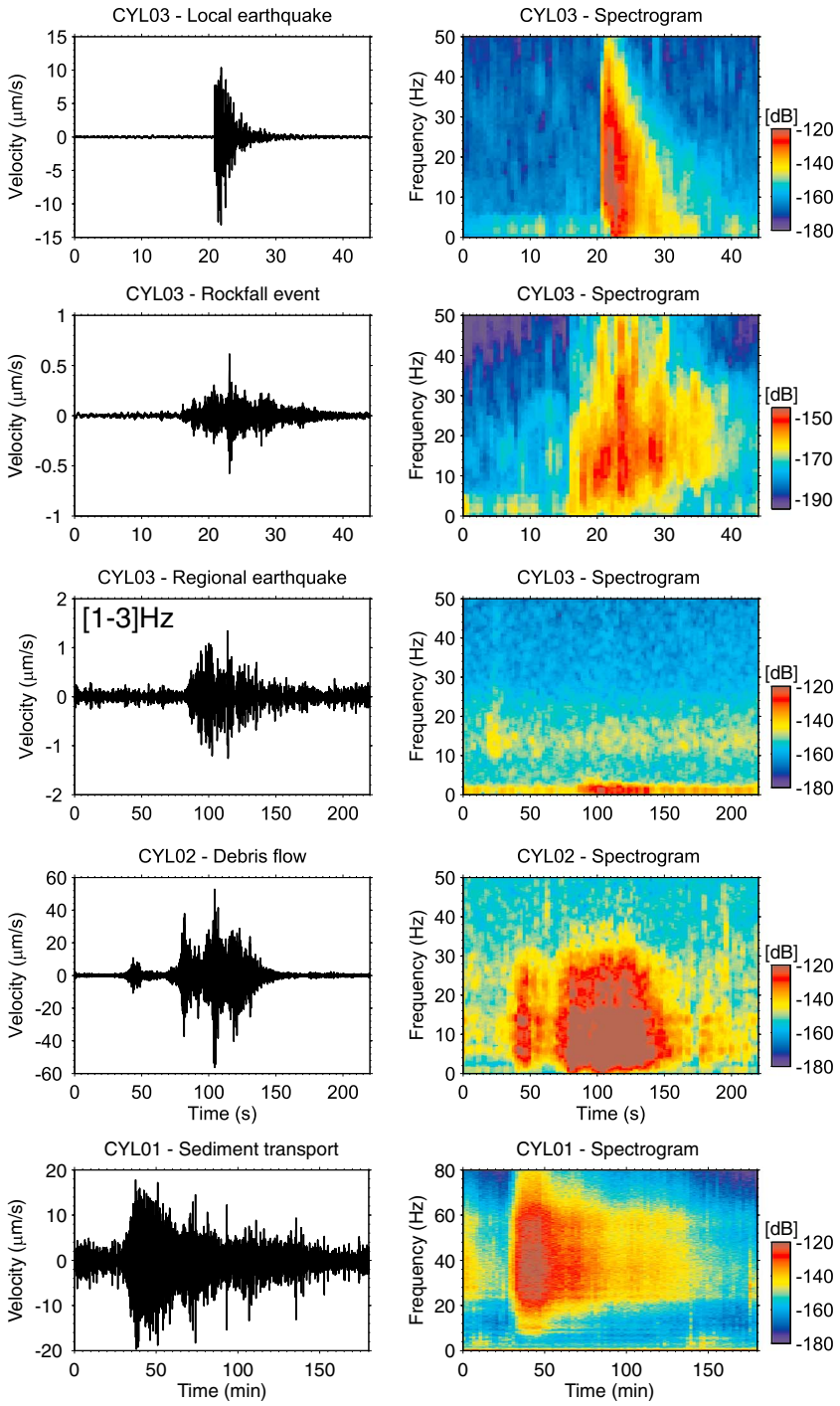

Figure 3. Seismic and spectral characterization of recorded events in the Chenyoulan catchment. (left) Vertical seismic signal in μm/s observed for a local earthquake, a rockfall (8 km from the station), a regional earthquake, a debris flow, and a bed load transport event, respectively. (right) Spectrograms computed from the corresponding seismic signals, showing the frequency-specific amplitude in dB relative to the velocity.

and to identify any erosion features smaller than 576 m^2. A further manual verification of mapped features was done with a composite of orthorectified photographs with a resolution of 0.5 m to determine the outlines of erosion features in the catchment at the highest possible resolution. Automated mapping and comprehensive manual checking did not show any new erosion features in the Chenyoulan catchment during the time interval of this study. This could be due to low geomorphic activity and/or the inability to detect all geomorphic change with this method.

3. Seismological Methods

3.1. Signal Classification

[12] Seismometers are sensitive to signals from a wide range of sources, including tectonic processes (earthquakes,

volcanic and nonvolcanic tremors), environmental sources (oceanic swell, ice movement, rainfall, and wind), and human activities. Although very large ($>10^7$ m^3), fast landslides can generate long-period wavefields that can be detected teleseismically [*Kanamori and Given*, 1982; *Ekström and Stark*, 2013], previous studies have established that the seismic signals emitted by common surface processes such as river bed load transport and rock avalanches are largely restricted to a high-frequency range (> 1 Hz) [e.g., *Burtin et al*., 2008, 2011; *Hsu et al*., 2011; *Dammeier et al*., 2011]. Unfortunately, this frequency band is also affected by local earthquakes (distances 100 km) [*Lay and Wallace*, 1995] and anthropogenic sources such as traffic, excavation, and construction work [*McNamara and Buland*, 2004]. A time-frequency characterization of a range of common event types is therefore required prior to the systematic analysis of geomorphic activity and its location. This does not exist at present, but some seismic characteristics of individual geomorphic processes can be identified from published work.

[13] During our survey, 29 shallow local earthquakes were triggered in the catchment with a magnitude range of M_l 0.7–5.7. Such earthquakes could be mistaken for riverbank collapses and rock avalanches. On a seismogram, a local earthquake typically exhibits a sharp rise of the seismic amplitude and the first wave arrivals are followed by an exponential amplitude decay. The event duration is related to the earthquake magnitude and is several tens of seconds (Figure 3). Seismograms of rock avalanches, recorded at various locations [e.g., *Deparis et al*., 2008; *Vilajosana et al*., 2008; *Hibert et al*., 2011; *Dammeier et al*., 2011; A. Burtin et al., Seismic constraints on dynamic links between geomorphic processes and routing of sediment in a steep mountain catchment, submitted to *Earth and Planetary Science Letters*, 2013, hereinafter referred to as Burtin et al., submitted manuscript, 2013], tend to have an emergent onset preceding the peak of amplitude, but the rise time varies from one event to another and also with distance to a station. The peak of amplitude tends to be followed by a more gradual decay of the seismic energy than for a local earthquake, but the two event types can have a similar duration (Figure 3). Moreover, variability of rockfall and rock avalanche rise times for a single event makes this parameter difficult to use for source characterization. As a consequence and when considered in isolation, the temporal features of seismic records for rock avalanches and local earthquakes are ambiguous. However, additional information can be obtained from frequency analysis. The spectrogram of a local earthquake commonly shows a sharp increase of the seismic energy over a broad high-frequency band (up to 40 Hz) [e.g., *Helmstetter and Garambois*, 2010], followed by an energy decay that is more pronounced at higher frequencies, illustrating the stronger attenuation of high-frequency seismic waves [e.g., *Toksöz and Johnson*, 1981]. A rock avalanche spectrogram also has a sudden or progressive onset, but the decay has a frequency dependence that differs from a local earthquake (Figure 3). First, we observe that the seismic energy below 3 Hz is not dominant as in earthquakes; second, we notice that the decay of energy is less important than for earthquakes; and third, there can be a shift to higher frequencies in the tail of rock avalanche signals recorded at relatively short distance from source [*Helmstetter and Garambois*, 2010; *Hibert et al*., 2011; Burtin et al., submitted manuscript, 2013]. We have used these frequency-specific attributes to distinguish between local earthquakes and rock avalanches within the reach of our instrument array.

[14] Larger earthquakes, located elsewhere in the region, are a second type of tectonic event recorded by the array. Most of these events were located in Japan and the Philippines, to the north and the south of Taiwan, respectively. The seismogram of a regional earthquake does not have a sharp rise in amplitude but rather shows a gradual increase over a few tens of seconds, followed by a gentle decay (Figure 3), giving an event duration on the order of 1 or a few minutes. These features are also common characteristics of debris flows that have a complex source time function with many peaks of amplitude [*Burtin et al*., 2009]. Amplitude-time analysis alone does not permit robust discrimination between tectonic and geomorphic events. However, our records of regional earthquakes are characterized by the absence of seismic energy above 5 Hz. This feature is probably explained by the anelastic attenuation of seismic waves that strongly affects the highest frequencies for large event-receiver distances (up to 1000 km) [e.g., *Toksöz and Johnson*, 1981; *Lay and Wallace*, 1995]. The observed spectrogram pattern for a regional earthquake thus results from the properties of the medium in which seismic waves propagate. Drastic high-frequency attenuations are not observed for sources located in the catchment. Therefore, debris flow signals have broader frequency contents and peaks of seismic energy in the 1–20 Hz band (Figure 3). Importantly, seismic waves from a debris flow do not usually propagate far. *Burtin et al*. [2009] found that a debris flow in the Himalayan Trisuli Valley with a volume of approximately 1500 m^3 registered at seismic stations up to 20 km away. In the Swiss Illgraben catchment, signals of smaller debris flows of about 1000 m^3 attenuated significantly within 5 km from source (Burtin et al., submitted manuscript, 2013). This is probably because the source is located at the surface, where the medium strongly attenuates the wave amplitude. In contrast, seismic waves from larger earthquakes ($M_w > 6$) at epicentral arc distances of 8–20° have been recorded by our array. This difference in characteristic travel distance gives a further means of distinguishing between debris flows and regional earthquakes. In addition to our own data, we have analyzed seismic data from permanent stations of the Broadband Array in Taiwan for Seismology (BATS) within 270 km from the Chenyoulan catchment (stations KMNB, TPUB, TWGB, SSLB, and YHNB), deeming any event within the catchment and observed at BATS stations to be tectonic rather than geomorphic in origin. However, it should be kept in mind that larger mass wasting events can have a distinct long-period signal, 10–30 s, that may be recorded at great distance [*Lin et al*., 2010; *Ekström and Stark*, 2013]. Smaller landslides produce seismic signals that last several minutes, sometimes up to tens of minutes, with high amplitudes, irregular envelopes, and a lack of distinctive arrivals of *P* and *S* seismic phases [*La Rocca et al*., 2004; *Suriñach et al*., 2005; *Favreau et al*., 2010; *Kao et al*., 2012]. The seismic energy is dominant in the 0.1–10 Hz frequency band but long-period waves can be recorded [*Favreau et al*., 2010].

[15] Shifting attention to environmental sources, river noise can mask the seismic signals of other processes. During floods, bed load transport of many particles simultaneously, flow turbulence, and air bubble cavitation can together produce a continuous seismic signal with long-term fluctuations associated with the river stage [*Burtin et al*.,

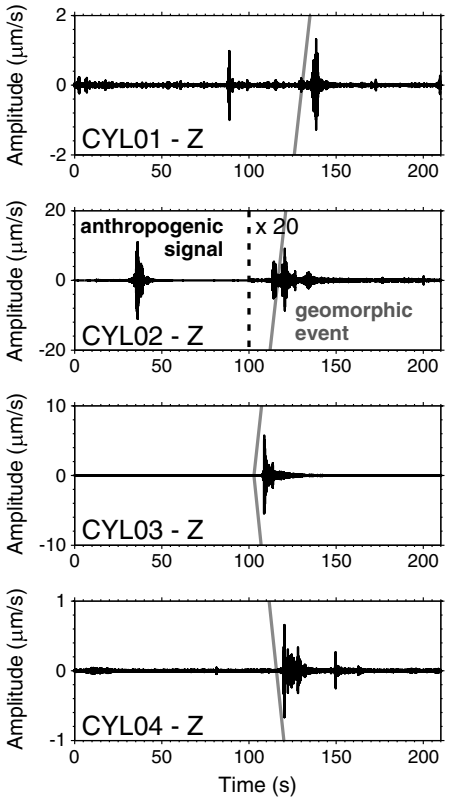

Figure 4. Comparison of an anthropogenic seismic signal with a geomorphic event (triggered on Day 194—time 08:36 A.M. UT) recorded at CYL01, CYL02, CYL03, and CYL04, from top to bottom, respectively. The vertical seismic records are band-pass filtered at 20–30 Hz. At CYL02, the amplitude in μm/s is 20 times increased after the dashed line at 100 s in order to observe the geomorphic event that is overwhelmed by the amplitude of anthropogenic event. The gray line highlights the arrival of the geomorphic event at stations. The anthropogenic disturbance is commonly only recorded at the nearest station whereas a relevant geomorphic event is detected by a large number of stations.

2011], occasional step changes due to localized sediment supply by hillslope mass wasting, and punctuations associated with the movement of individual, large grains, or sets of grains [*Turowski et al*., 2009] (Figure 3). The multitude of bed load impacts in a mountain river may induce overlap of seismic waves, which precludes the identification of individual particle-bed collisions and gives rise to a continuous seismic signal of bed load transport. In our survey catchment, flooding of the Chenyoulan River could generate high-frequency signals, mainly above 20 Hz (Figure 3). Seismic stations located in the vicinity of the Chenyoulan River and its tributaries might therefore, at times, be overwhelmed by river signals, affecting our ability to detect and locate small rockfalls. However, larger mass wasting events and earthquakes have sufficient energy to emerge from the river signal. Moreover, the river signal is distinct from most others due to its continuity, with possible exception of wind and rainfall. These sources also affect the spectral energy of seismograms above 1 Hz [e.g., *Withers et al*., 1996], where wind disturbance is enhanced at stations in the vicinity of trees whose roots transfer wind energy to the ground. Therefore, we have avoided the installation of stations close to tall trees. Seismic noise from rainfall is unlikely to affect our data significantly. In a previous study in a river braid plain in the French Alps, *Burtin et al*. [2011] noticed that rain only affects the seismic data from stations that were located close to large boulders. In contrast, stations situated in finer-grained sediments, a few hundred meters away from these boulders, did not register rainfall. This indicates that the coupling of raindrops with the ground may only be efficient on rocky substrates. In the Chenyoulan, our stations were systematically located in colluvium or alluvium. Furthermore, *Burtin et al*. [2011] found that the seismic noise from rain was dominated by frequencies >60 Hz and had no coherence between stations.

[16] Finally, human activity is a frequent source of seismic signals [e.g., *McNamara and Buland*, 2004]. In the configuration of our array, we have suppressed this class of signals by avoiding as much as possible roads, pipelines, settlements, and farms as well as temporary works. In the mountain setting of our study catchment, farming, construction, gravel extraction, and traffic are the main activities. Largely confined to daylight hours, these activities tend to give punctuated seismic signals, with a high-frequency content that attenuates quickly with distance traveled. Moreover, the energy of the anthropogenic sources in this setting is typically small and is mostly registered at only one or two stations. For example, cars passing near station CYL02 register at that station with an amplitude of about 10 μm/s (Figure 4), but not at other stations in our network. Also, station SHP04, located about 0.2 km from the Chenyoulan River (Figure 1), recorded anthropogenic disturbances due to gravel extraction from the river bed (Figure S1 in the supporting information). The seismic record of this station shows a succession of short impulse events that are produced by pneumatic tools that we observed during station maintenance visits. At the nearest station CYL08, 2 km from SHP04, such seismic signals were not recorded. These examples highlight the fact that many human sources of seismic signals are only effective in close proximity of a station and could not be registered at multiple sites elsewhere in our array. By imposing a minimum number of stations at which an event is recorded, these sources can largely be excluded from further analysis. This may result in the exclusion of small geomorphic events from detection and location. Figure 4 shows that the anthropogenic event in the vicinity of CYL02 was followed by, and contrasted with a possible geomorphic event that was detected by all stations of our array.

[17] Taken together these observations underline the importance of combining the frequency, time and attenuation characteristics of an event signal to discriminate between source types. In the absence of quantitative criteria for most source types, we have done this manually. The identification of such criteria remains an outstanding challenge in the development of this approach.

3.2. Signal Detection

[18] Over a longer-term survey, the total number of recorded events can be such that comprehensive manual detection and location become impractical. Moreover, manual analysis precludes objective, continuous, and, ultimately, real-time monitoring. Therefore, we have applied an automated approach to the detection and location of events.

[19] Our automated event detection uses a short-term average/long-term average (STA/LTA) approach [e.g., *Havskov and Alguacil*, 2006]. This method is widely used in

seismology for the real-time survey of seismicity recorded by permanent seismic networks. The detection algorithm considers the ratio between the average of the absolute seismic signal over a short- and a long-time window of about 1 and 100–500 s, respectively. An event is identified when the STA/LTA ratio exceeds a predefined threshold for more than a predefined length of time. The seismic signals of expected geomorphic events have a range of characteristics: (1) signals with a short duration (10^1 s; Figure 3), possibly induced by bank erosion, debris mobilized in gullies or rockfalls, and (2) complex signals with a longer duration (10^2 s; Figure 3), maybe generated by debris flows, rock avalanches, or landslides. Because the duration of an event affects the LTA and the duration of the detection trigger, we have defined two different sets of parameters for the detection of these two types of events.

[20] Prior to execution of the detection algorithm at a station, the three component seismic records were first deconvolved from the instrument response, and we removed the trend and the mean of the time series. Subsequently, we used a band-pass filter with a 20–30 and 1–4 Hz frequency band for the detection of fast mass wasting processes and debris flows or landslides, respectively. These frequency bands were chosen in accordance with the observations summarized in section 3.1 and with the express aim of singling out geomorphic processes other than bed load transport. The 20–30 Hz band is narrower than the characteristic frequency range of fast mass wasting processes. However, at lower frequencies, the amplitude envelope of recorded signals is too complex, with too many individual peaks and too little difference between peak and background energy. At higher frequency, the definition (weight) of the peaks is better, but the signal attenuation is too strong to guarantee detection at multiple stations. Moreover, signals lose coherence between stations at higher frequency, which becomes problematic above 40 Hz. The 20–30 Hz band pass is a compromise between these two. Furthermore, we opted for a 1–4 Hz band pass for the detection of debris flows, because the seismic signals of these flows can exhibit important discrepancies between stations at frequencies >5 Hz as well as complexities in the time history [e.g., *Arattano and Marchi*, 2005; *Burtin et al*., 2009] that can affect the length of the detection trigger. Once the seismic data were filtered, we summed the absolute amplitude of all available components at a station and ran the detection algorithm on this function.

[21] The length of the STA was set at 1 and 10 s and the LTA at 120 and 300 s, for the short- and long-time event detections, respectively. The threshold ratio to trigger the detection of an event was set at 3 and we used a detrigger threshold of 1.5 [*Havskov and Alguacil*, 2006]. A long-duration event might affect the LTA, compromising the characterization of the background noise level of the time series. Therefore, we have used a freezing LTA after exceedance of the trigger threshold. Finally, and in accordance with preliminary event observations (Figure 3), the minimum-required duration of the trigger was set to 15 and 50 s for the detection of short- and long-time events, respectively. Use of shorter trigger times would permit detection of smaller, local events, with increased likelihood of spurious results due to numerical noise, and longer trigger times would give rise to unwanted exclusion of some significant geomorphic events.

3.3. Signal Location

[22] To locate surface and near-surface sources, we have employed a method developed for the monitoring of nonvolcanic tremors. It is derived from the source-scanning algorithm (SSA) introduced by *Kao and Shan* [2004] and uses the full time evolution of seismic amplitude during an event. We used this algorithm because the identification of a coherent first arrival at many stations is usually impossible. The principle of the approach is to map in a medium the absolute seismic amplitude recorded at a station, for a given initial time and velocity model. This migration of the seismic amplitude is then produced for all stations, and the event location is found by looking for the largest peak amplitude since a coherent signal at stations should culminate at a shared point, the origin of the event. The procedure has two main stages: (1) the calculation of the amplitude function for each station and (2) the migration of these functions to compute a brightness function [e.g., *Kao et al*., 2012].

3.3.1. Amplitude Function

[23] First, to simplify the processing of data with different sampling rates, we reduced the 200 SPS signals of the GURALP sensors to 100 SPS. Then, for each event and each station, we defined the amplitude function as the sum of the absolute amplitude of all available components. We then applied a 1 s smoothing window to the amplitude functions. This corresponds to the weighting factor W_m in *Kao et al*. [2012], fixed at a value of 1. For a set of smoothed amplitude functions, we then calculated the signal to noise ratio (SNR) in order to determine the quality of the seismic data before migration. In our study, this SNR criterion corresponded to the ratio of the peak amplitude over the average of the amplitude function and we assumed that this average was representative of the background noise level. We selected signals with SNR value greater than 3.5, to eliminate recordings with background seismic noise that could affect the location. Finally, the viable amplitude functions were normalized by 2σ (standard deviation of the time series), emphasizing seismic signals with a high SNR [*Kao et al*., 2006]. In principle, the location of a surface source can be retrieved with records from only three stations. However, in practice, the properties of our seismic array and the quality of our data stipulate that the errors on a location are optimal with data from at least five stations. Therefore, we have only considered events that were observed at five or more stations.

3.3.2. Migration Procedure

[24] To determine the likely location of a recorded event with a source at or near the Earth's surface, we have migrated the corresponding amplitude functions $U^A(t)$, using a ballistic propagation with a constant velocity V in a discrete medium $M(x,y)$, where x and y are the spatial coordinates relevant to the location process. In this procedure, time t was expressed as $t_0 + \tau$, the initial time of the event plus the propagation time from its location to a station i situated at x_i, y_i:

$$\tau_i(x,y,z,V) = \sqrt{(x-x_i)^2 + (y-y_i)^2}/V.$$

[25] Hence, for an assumed t_0 and a set of N stations, the migration of each seismic signal was expressed as

$$M(x,y,V,t_0) = \sum_{i=1}^{N} U_i^A(t_0+\tau_i)/N.$$

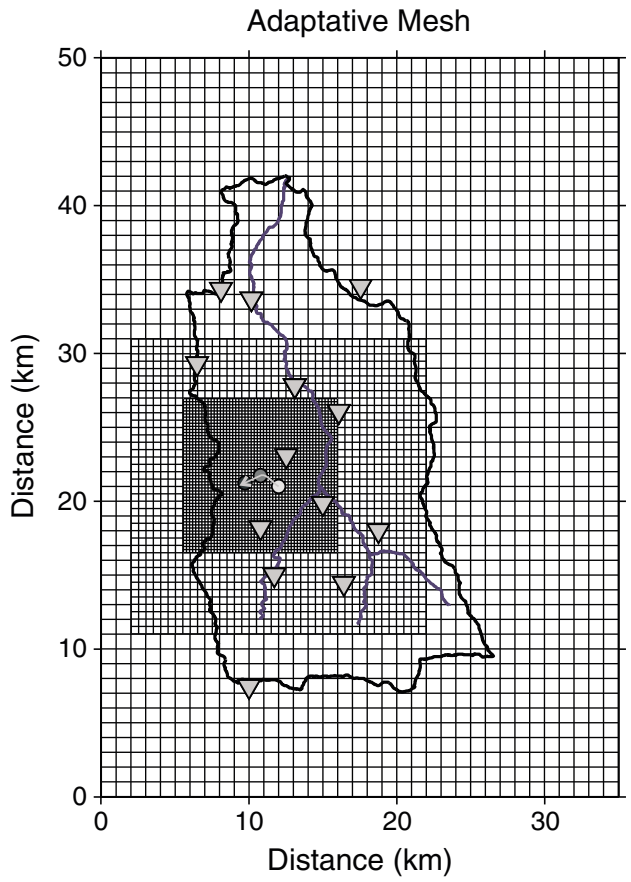

Figure 5. Illustration of the adaptive medium discretization used in the location procedure. A higher-resolution grid is introduced around the last best location to improve the best fit solution and to save computation time. A similar adaptive discretization of the event initial time is used but is not represented here. Note the progression of best location solutions with an increasing resolution, shown by circles from light to dark gray tone. The seismic stations of our array are shown by inverted triangles, and the outlines of the Chenyoulan catchment are shown in black.

[26] In this treatment, $U_i^A(t_0 + \tau_i)$ can be interpreted as the retropropagation of the seismic signal. Therefore, the amplitude $U_i^A(t_0)$ is associated with the cell of the medium where station i is located. As a result of the migration procedure, the highest peaks of amplitude recorded at each station should merge at the origin of the event under consideration. The best fit location of the event is at the maximum of M. It must be stressed that this migration process does not fully take into account the heterogeneity of the local velocity structure and the details of the wave path.

[27] In practice, we did not have sufficient independent constraints on the velocity V of high-frequency waves in the substrate of the Chenyoulan catchment. Moreover, event time t_0 was unknown. With these two unknown parameters and the unknown spatial coordinates x and y of the event location, a detailed exploration is very time consuming. To reduce the time of data processing, we applied a sequential procedure with three steps, in which the resolution of the unknown parameters was progressively increased. We set the grid increment dl to 1 km initially, and changed it to 0.5 km and then 0.1 km in two further steps. In parallel, the area of exploration was decreased to 20 km^2 and then 10 km^2 around the best location in the previous analysis step. This stepwise focusing of the location procedure is illustrated in Figure 5. Although theoretically possible, in our study, the formal best solution was on no occasion located outside the grid area selected in the initial reduction step. Our method has limited sensitivity to the depth parameter, but in the case of geomorphic events, most of the activity is located at the Earth's surface, or at shallow depths ($<10^2$ m). Given this, the event depth could be fixed at the surface. In addition, the ballistic migration does not take into account the topography of the medium. The difference between the raypath distances in a flat medium and one with topography is limited (Figure S2), about 1.8% for the studied region in its entirety and areas with more than 10% difference only represent 0.6% of the medium.

[28] A stepwise approach was also used for estimation of t_0, reducing the tested values progressively from ±40 to ±5 s around the best solution of the previous step. The time resolution dt was adjusted with the grid resolution dl and the assumed propagation velocity V according to dt = dl/V. To retrieve the velocity, we explored a range of ±0.2 km/s around the best solution from the previous best fit velocity, starting with arbitrary values of V = 0.5 and 2.0 km/s for the high- and low-frequency wave contents, respectively. These starting values were chosen in view of test events and previous experience [*Burtin et al.*, 2009; *Helmstetter and Garambois*, 2010]. They do affect the efficiency but not the outcome of our procedure.

[29] Finally, to check the coherence of the location result, the algorithm was executed again, starting with the parameters of the best solution from the initial cycle. This control of best fit parameters was stopped once the final solution had stabilized. It ensured the elimination of any spurious focus on local maxima due to the low spatial and temporal resolutions at the outset of our analysis. In practice, the explored regions with higher resolution were quite large and most solutions were confirmed already in the second cycle.

[30] Some location examples for different event types are illustrated in Figure 6. The results take the form of a brightness map, with rings of high amplitude centered on stations with the highest SNR. Depending on the complexity of the seismic records for individual stations and the velocity field, most of the amplitude peaks or rings on the map should coalesce in a relatively small area. The degree of coalescence reflects to a first order the quality of the location estimate. In the examples in Figure 6, red lines mark the theoretical arrival times of the dominant waves that we would expect to observe with the best velocity and location.

3.3.3. Error Estimate

[31] A brightness map gives an event location and a pattern for its precision. The brightness patterns differ from one event to another due to the event position relative to the stations in a heterogeneous medium and other influences on the quality of the seismic data. In order to interpret the location results as a single data set, a realistic location error must be defined that takes in account the assumptions associated with our approach. In the absence of controlled active sources, we have compared the locations of 29 shallow (<10 km) local earthquakes within the Chenyoulan catchment derived by our method against independent locations reported by the CWB for these same events, to define a location precision. The posted horizontal and vertical

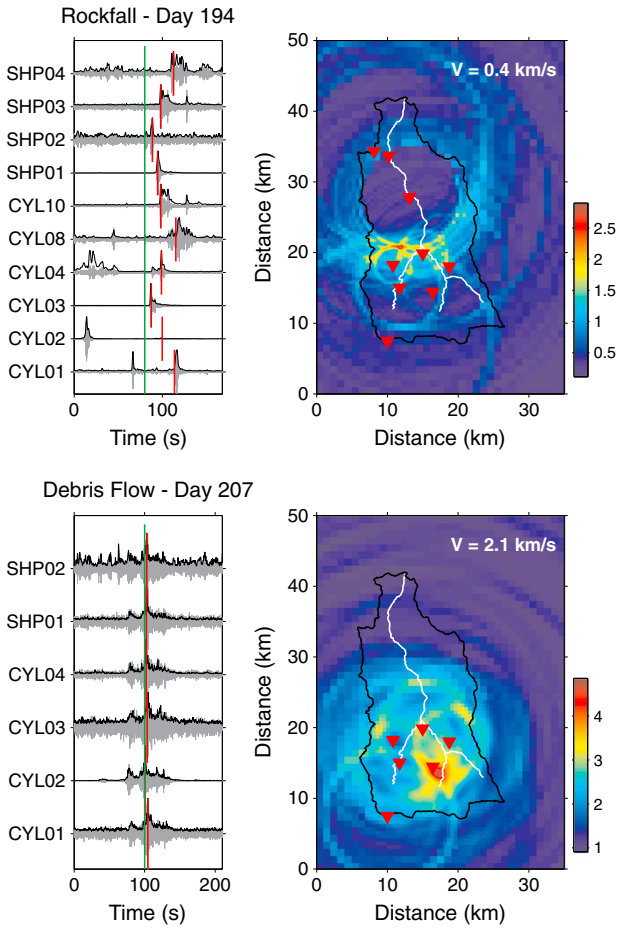

Figure 6. Event location of (top) a rockfall (Figure 4) and (bottom) a debris flow. On the left side, vertical seismic signals (gray) and absolute amplitude functions (black) of the located event are graphed. The green lines demarcate the initial time of the located source and the red lines mark the theoretical arrival time for the best location and velocity. On the right side, the location maps illustrate the migration of the absolute amplitude functions for all stations. The coherence of migrations is shown in the color scale, which is normalized to the standard deviation of amplitude functions. The red areas mark the best fit location of the events for the best fit velocity (V) as given on the map. Inverted red triangles show the seismological stations used in the respective locations. The outline of the Chenyoulan catchment is shown in black, and its trunk streams are shown in white.

errors on these reported locations are 0.6 and 0.8 km, respectively. We filtered the seismic signals in the 1.5–6 Hz frequency band that offered the best compromise for the ensemble of events. This range of frequencies is similar to that selected for location of debris flows, but lower than the frequency range targeted for location of fast mass wasting events. In this higher-frequency range, the quality and complexity of earthquake signals do not permit use of our location approach. Locating events with a lower frequency content uses broader amplitude peaks that give bigger bright areas with relatively large uncertainties. Therefore, our constraints on location uncertainties are conservative. After filtering, we followed the procedure as described in preceding sections. The two independent sets of earthquake locations were in significant agreement (Figure 7). For the 29 local earthquakes, the mean horizontal mismatch between independent locations was 2.4 ± 1.3 km and it never exceeded 5 km. If it is assumed that the CWB locations are absolutely correct, then this mismatch could define a minimum precision of our event locations. For the best fit velocity, we obtained a value of 3.1 ± 0.3 km/s, which seems realistic since the highest amplitudes should be related to shear and/or surface waves. This value is higher than the 2.1 km/s found for the debris flows highlighted in Figure 6, even though the migration was done with a similar frequency content. The velocity discrepancy probably arises from the depth of the sources and/or from the nature of the wave at the point of focusing. For an earthquake at a depth of ~5-10 km, the high-frequency waves propagate at greater depths and presumably at higher velocities than for a geomorphic event at the surface.

[32] In seismology, it is common practice to report locations with uncertainties <5% of the dynamic range of brightness [e.g., *Lacroix et al.*, 2012]. Acknowledging, the minimum precision of our event locations as constrained by the analysis of local earthquakes, we have imposed a more conservative, arbitrary threshold of 22%. At this threshold, we can match the CWB locations of 50% of the local earthquakes as resolved from the brightness function. Accordingly, event locations are reported within the grid area with normalized brightness values >0.78. This area typically has an elliptic shape around the brightness maximum. The ellipse can be described by two orthogonal, principal axes of different lengths defining an area

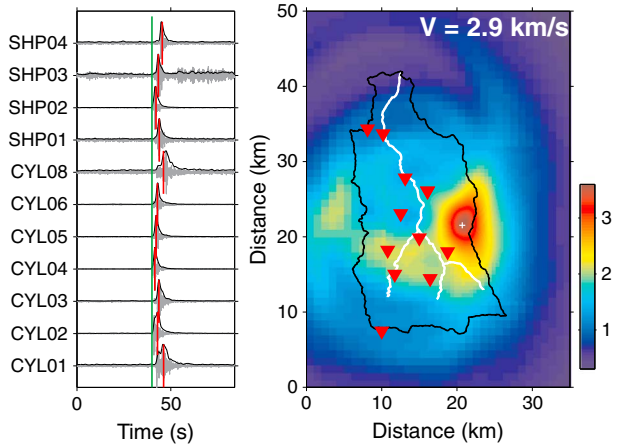

Figure 7. Example of a M_l 1.1 local earthquake (triggered on Day 219—time 10:02 P.M. UT) processed to determine a realistic error for the location approach. On the left side, vertical seismic signals and absolute amplitude functions of the located earthquake are graphed for all seismological stations in our local network. The green lines demarcate the initial time of the located source and the red lines mark the theoretical arrival time for the best location and velocity. On the right side, the location map shows the coherence of the absolute amplitude functions for all stations. The area with the highest coherence is most likely to contain the earthquake epicenter. This coincides with event location published by the Taiwan Central Weather Bureau, for which the residual horizontal errors are shown by white bars.

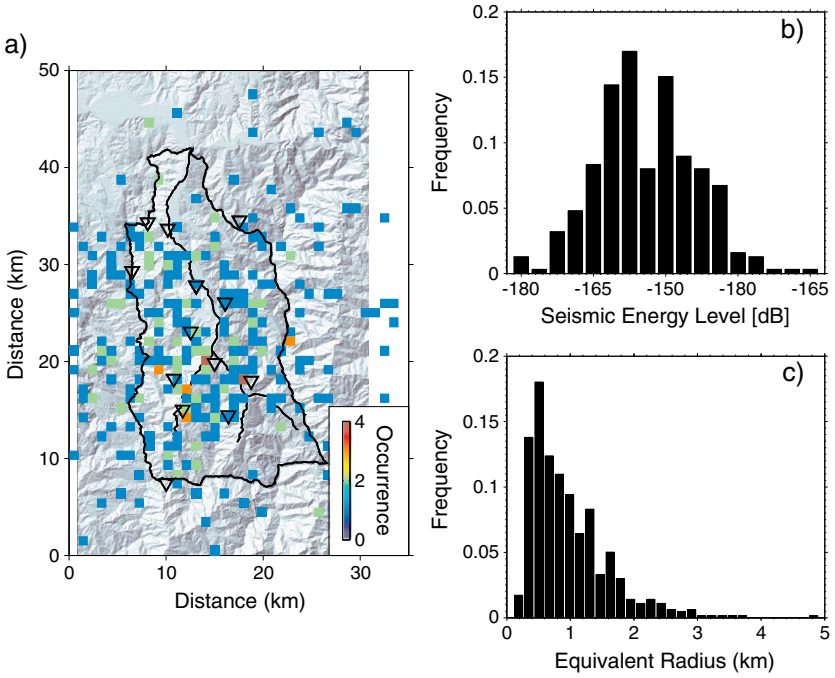

Figure 8. (a) Distribution of 314 seismologically detected and located geomorphic events in the study area gridded at 1 km resolution, with number of events per grid cell shown in color. The detected events were widely distributed in and around the Chenyoulan catchment. (b) Frequency distribution of seismic energy and (c) equivalent radius of uncertainty for the located geomorphic events. The average seismic energy was −163 dB and the average and modal radii of uncertainty were 1.0 and 0.6 km, respectively.

of confidence for the event location. The radius of a circle with a surface area equal to that of the uncertainty ellipse for an event was 1.0 km on average for the population of high-frequency events, with a significantly lower modal value of 0.6 km (Figure 8). The average and modal length scale of uncertainty are equivalent to 9% and 5% of the average distance between stations in our array, respectively. Full brightness maps can have secondary maxima with values <0.78 outside the location uncertainty ellipse.

4. Results

4.1. High-Frequency Seismic Signal

[33] A time-frequency analysis of seismic data for the duration of the survey highlights the seismic energy from near-surface sources within the area covered by our array. As an illustration, the spectrogram for station CYL01 at the head of the catchment shows episodes of seismic energy that coincided with rainfall peaks (Figure 2), in particular, the tropical storm on Days 207–209 and Typhoon Fanapi on Days 261–262. Other peaks of the average seismic energy in the 1–80 Hz frequency band (Figure 2) were also apparently coincident with rainfall. In addition to these prolonged episodes of activity, daily sharp peaks of seismic energy between −180 and −165 dB have been recorded at station CYL01. From Days 192 to 208, this periodic signal was uninterrupted, and it was repeated in other shorter sequences until the end of the survey (Figure 2). These periodic bursts of activity occurred during afternoon convective storms, which are typical in tropical mountain regions. They were particularly well expressed at CYL01, probably because of the elevation of that station, 2327 m asl and associated orographic effects on precipitation. The bursts of high-frequency energy recorded in the Chenyoulan catchment resemble the seismic signals of slope and river processes registered elsewhere [e.g., *Burtin et al.*, 2009, 2011].

4.2. Location of Near-Surface Events

[34] Applying the criteria and protocols outlined in section 3.3, we have located 314 events with a likely near-surface source in the interval July–September 2010 (Figure 8). The large majority of these events were located within the catchment, but 89 near-surface events outside the watershed were registered by our seismometer array. The detected events were widely distributed, with an average distance between an event and the nearest station of 4.9 ± 3.9 km and a maximum of 42 km. The fact that the average event distance to the nearest station is similar to the average half-distance between stations, 5.5 km, confirms that our results are not substantially biased by short-distance attenuation of seismic signals. Spatial clustering of events was limited. Although 141 events are likely to have occurred within 1 km from at least one other event, only 63 events had two or more neighbors within this distance. Insofar as the errors and uncertainties on event location permit an assessment, the events occurred across a range of topographic settings including steep stream banks, small tributary channels, straight hillslopes, and ridge crests. Event clusters were found near steep-walled trunk channels and on steep headwalls of geomorphically active tributaries.

[35] The signals of 312 located events were dominated by the high-frequency content that we have tentatively attributed

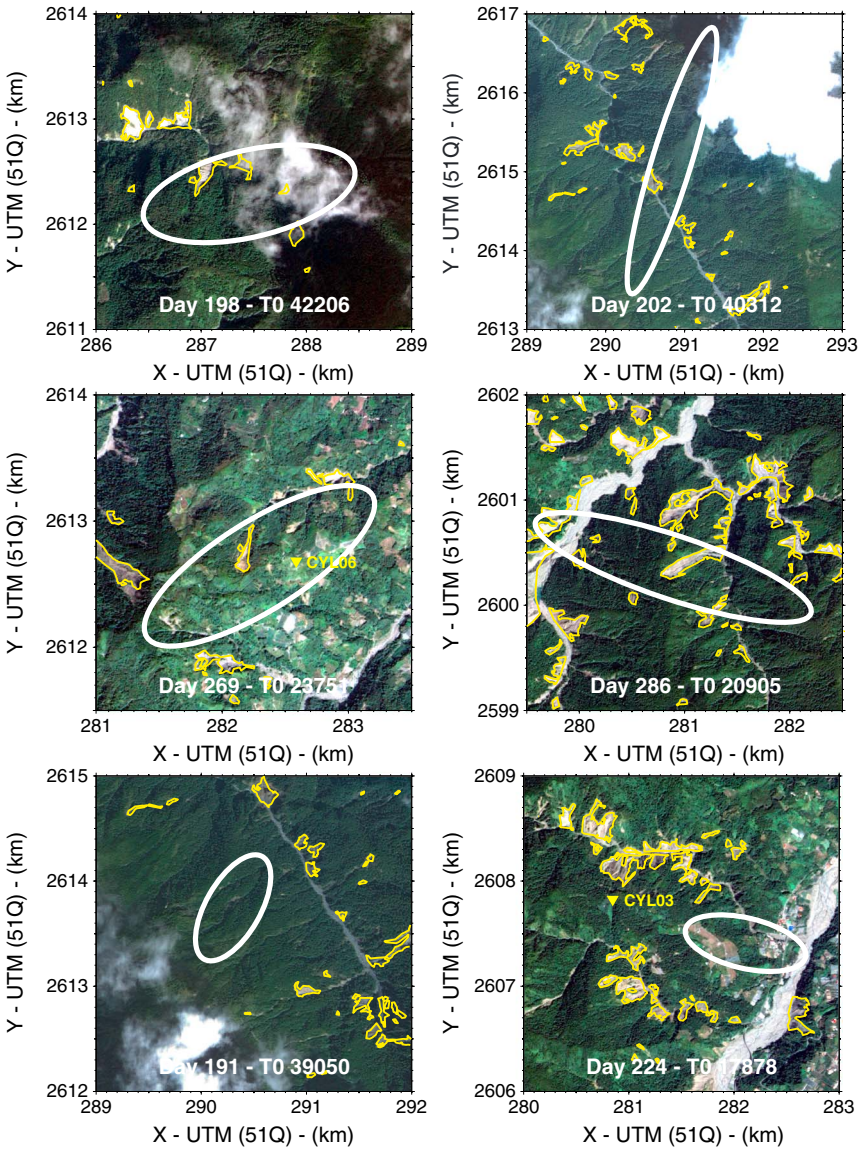

Figure 9. Visual observation of geomorphic event locations. Seismologically determined event locations are shown, using their respective uncertainty ellipses, projected onto FORMOSAT-2 panchromatic images with a spatial resolution of 2 m, taken after the detected events had occurred. In many cases, the seismologically detected events could be associated with active geomorphic structures (yellow), such as landslide scars or gullies that predated the events. In some cases (examples shown in bottom row), the event locations did not match with a clearly visible geomorphic structure.

to fast mass wasting processes such as rockfall and rock avalanching. The energy level at 20–30 Hz of these events, averaged over the three stations nearest to the likely event location ranged from −180 to −139 dB, with a mean of −163 dB (Figure 8b). These levels of seismic energy denote events that are likely to have a limited size. Geomorphic events recorded by the Hi-CLIMB array along the Trisuli River ranged from −151 to −133 dB [*Burtin et al.*, 2009]. The mean seismic amplitude of events observed in the Chenyoulan catchment was 4 times smaller than the smallest event studied with the Hi-CLIMB data set. Since the source to station distances were similar in these two studies and in view of their shared mountain setting, we tentatively attribute differences in signal strength to the likely small size of events recorded in the Chenyoulan catchment. Lacking a wave attenuation model for the catchment, we abstain from a conversion of recorded energy levels into source energy.

[36] In addition to these high-frequency events, two events were detected with a dominant signal in the 1–5 Hz range. Both occurred during the first day of the tropical storm in July (Day 207; Figure 2). The event durations were short, 1 to a few minutes, but with several peaks of high amplitude, resulting in a complex source time function (Figure 6). The absence of low-frequency signal content and the proximity of the sources to channels are suggestive of debris flow, although a landslide source is difficult to discard. We tried to locate these events with a high-frequency band, as for the short duration events (20–30 Hz), but the constraints on

location were not satisfying. Difficulties with the location of debris flows are due to the complexity and long duration of seismic signals from mobile sources that preclude sufficient coherence between stations. The presence of multiple peaks in the absolute amplitude function of a debris flow signal gives rise to ambiguities when they are added in the brightness function.

[37] For near-surface events with a high-frequency content, the velocity at 20–30 Hz was around 0.4 ± 0.1 km/s (data from 312 events). The relative uniformity of these best fit velocities for widely distributed sources suggests that this narrow velocity range is representative of the substrate throughout the catchment. Location tests with amplitude functions made from a separation of the vertical component and the quadratic sum of horizontal components did not significantly change the results. The relative weight of horizontal components is thus larger than the vertical component and most of the seismic energy should be carried by shear and/or surface waves. However, robust estimation of the vertical component is difficult since the 1 s smoothing applied to the vertical and horizontal amplitude functions attenuates the possible disturbance of *P* waves on *S*, Rayleigh, and Love waves. A particle motion analysis could be used to elucidate this issue but was outside the scope of this study. Therefore, assuming that most of the seismic energy was due to surface waves with a small penetration depth at high frequencies, low velocities are thought to reflect the characteristics of very shallow substrates, including intensely fractured rocks, regolith, soil, and unconsolidated sediment [*Clarke and Burbank*, 2011]. Independent measurements of surface wave velocities at two high mountain locations at the edge of the Chenyoulan catchment found $V_s > 0.76$ km/s [*Lee and Tsai*, 2008], at the top end of the range of best fit velocities for the near-surface events detected in and around the catchment. If the difference in surface wave velocity between these two stations and the bulk of the Chenyoulan catchment is real, then it could reflect the concentration of very weak materials such as colluvium and alluvium, with very low V_s values, in lower positions in the landscape and dominance of weathered bedrock with slightly higher V_s values near ridges.

[38] The location method we have used explains most of the peaks of amplitude observed at stations. However, the agreement is lost for the stations farthest removed from the likely event location, as shown for a rockfall event recorded by stations CYL01 and CYL08 (Figure 6). Hence, over larger distances (>20 km), the assumption of a constant velocity fails to capture the heterogeneities in substrate characteristics. For the low-frequency (possible debris flow) example in Figure 6, the location estimate was derived, unsurprisingly, from the largest amplitudes observed at stations. In that example, the relatively low SNR values of the distant stations did not adversely affect the ability to retrieve a tightly constrained solution. Thus, the method seems to provide good estimates of the location of both brief events with a high-frequency content and longer-lasting events with a lower frequency content.

4.3. Comparison With Imagery

[39] To investigate the link between our seismic event observations and geomorphic activity in the catchment, we used FORMOSAT-2 multispectral images (8 m resolution) and orthophotographs (0.5 m resolution). We performed an analysis of available images to detect change in the shape of erosion scars and to identify new events. In contrast to preceding years with markedly high rates of mass wasting in the catchment, five satellite images of the Chenyoulan catchment with less than 6% cloud cover, acquired between August and October 2010 did not reveal the occurrence of any visible erosion events, neither landslides nor debris flows. Even passage of Typhoon Fanapi did not cause visually detectable change due to erosion in the catchment. Systematic manual checking of all areas with significant prior geomorphic activity, using the 2 m resolution panchromatic version of FORMOSAT-2 images, also did not reveal substantial visible activity on hillslopes and confirmed the results from the automated detection procedure.

[40] Notwithstanding the lack of discernable geomorphic change over the survey interval, we have seismically detected at least 314 events with a near-surface source, most of which were located well away from anthropogenic activity. If these events had geomorphic sources, then they may have remained invisible to us for several reasons. Geomorphic sources may have been located within areas already devegetated by prior erosion, precluding optical detection by a method predicated on changes in vegetation cover. Comparing the locations of seismically detected events with available imagery (Figure 9), we have found that 61% of detected near-surface events were collocated with major erosional features such as landslide scars or gullies that predated the survey interval, within the uncertainty of our location (modal value of 0.6 km). Only 40% of the catchment surface area fits this distance criterion. Using a Monte Carlo approach, the likelihood of randomly drawing 61% of 314 events matching a search criteria from a population of which 40% match this criteria in 10,000 attempts is 1×10^{-12} (Figure S3). From this we conclude that preferential event location within an existing erosion scar can have been a significant cause of our inability to identify them on remote-sensed imagery. However, for 39% of detected events, no direct link was found between the event location and an existing geomorphic feature (Figure 9). This could be due to erroneous event recognition or location. Alternatively, some geomorphic sources may have been smaller than the unit of change detectable with FORMOSAT-2 multispectral data (64 m^2). Others may have been obscured by forest cover. Furthermore, seismic surveying can detect rockfall in very steep topography, where the process is difficult to assess from imagery taken at a vertical angle. And finally, geomorphic sources may have been hidden by cloud cover, but this only affects 18 detected events.

[41] Thus, we have no direct evidence of the nature of the seismically detected near-surface events. These events have seismic characteristics that match those of geomorphic processes, such as rockfalls, fast debris slides, and debris flows, but could also be due to nongeomorphic sources. If the detected events were geomorphic in nature, then they remained invisible on available remote sensed imagery due to their small size, location within existing erosion scars or very steep slopes, and/or overhead cover. Nevertheless, we do propose that the majority of detected near-surface events were likely geomorphic in nature. Our principal evidence for this is circumstantial, consisting of a tight link between the detected events and the spatial and temporal patterns of

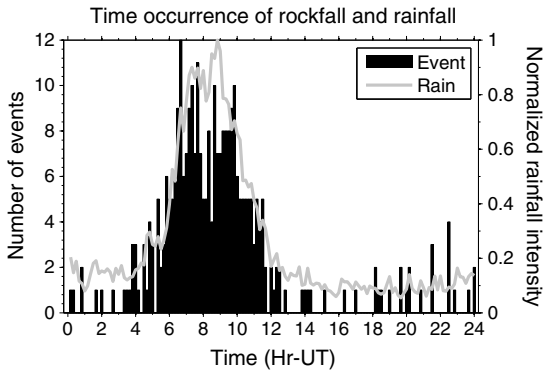

Figure 10. Comparison of the daily time distribution of rainfall (gray) and the occurrence of seismologically detected and located near-surface events (black). For each day with convective precipitation, 10 min rainfall rates were averaged for the 16 stations in our study area and then normalized to the maximum average rate for the day. The gray line represents the average rainfall distribution for 88 days with convective precipitation. Both data sets show a coherent time variation with most activity (rainfall and geomorphic events) occurring between 06 A.M. and 11 A.M. UT (02 P.M.–07 P.M. local time).

precipitation in the Chenyoulan catchment. This is substantiated in the next section.

5. Links Between Detected Events and Rainfall

5.1. Event Patterns in Time and Space

[42] Rainfall is a universally recognized driver of geomorphic activity. Therefore, if the seismically recorded near-surface events are indeed mostly geomorphic in nature, then it is expected that their patterns should be correlated with rainfall in the Chenyoulan catchment. Before we consider this further, it is important to rule out other possible mechanisms that could give rise to links between rainfall and seismically recorded activity. Meteorological phenomena such as rainfall, wind, and thunder can register on seismometers. However, due to their duration and frequency content, rainfall and wind can be ruled out as sources of the 314 recorded events discussed in section 4. Thunder during heavy rainfall has a duration more like that of the detected high-frequency events, but atmosphere-ground coupling is most effective at frequencies below 15 Hz [*Kappus and Vernon*, 1991; *Scarpetta et al*., 2005], which is at the lower end of the characteristic frequency range of these events. Moreover, the seismic signal of thunder is typically limited to distances below 5 km [*Kappus and Vernon*, 1991; *O'Connell-Rodwell et al*., 2011]. As we require an event to be recorded by at least five stations for detection, this short attenuation distance implies that thunder can also be excluded as a significant source of near-surface activity identified by our network. Furthermore, it has been argued that rainfall may affect the occurrence of earthquakes, either by downward fluid diffusion from the surface [e.g., *Bollinger et al*., 2007] or by erosional unloading of active faults [e.g., *Wdowinski and Tsukanov*, 2011], but these mechanisms require exceptional or very prolonged precipitation and they are likely to entail significant delays between the meteorological driver and seismic response of up to years. For these reasons, we also rule out rainfall-triggered seismicity as a possible source of the near-surface activity we have detected. Finally, we assume that human activity in rural mountain areas is negatively affected by precipitation and that we have not overlooked any other sources of high-frequency seismic signals that are systematically activated by rainfall. With this in mind, we look first at the temporal and then the spatial links between precipitation and seismically detected events.

[43] To explore temporal links, we have computed the characteristic daily rainfall distribution by first combining and averaging the 10 min records from all 16 stations in the catchment (Figure 1) and then normalizing each day to the daily maximum rainfall rate. This normalization gives equal weight to days with different precipitation rates, thus allowing a clean focus on the temporal aspect. By averaging the time distribution of rainfall for all days without a dominant cyclonic weather system, we then obtained the typical daily time distribution of rainfall in the catchment (Figure 10). This distribution shows a strong and regular periodicity with most rainfall between 2 P.M. and 7 P.M. local time (6 A.M.–11 A.M. UT) due to local, convective storms. A coincidence of this rainfall pattern with the seismic energy recorded by stations in our array was already noticed from the initial spectral analysis of the seismic data (Figure 2). Indeed, the time distribution of seismically recorded events has a very similar daily periodicity with 69% of events occurring in the afternoon rainfall hours that make up 20% of the day (Figure 10).

[44] An analysis of average 10 min rainfall rates at the three meteorological stations closest to a recorded event (Figure 11) shows that activity of near-surface sources coincided mainly with peak rainfall rates during storms. Taking into consideration the rainfall during 12 h either side of a recorded event, the kurtosis Kurt of the rainfall time-intensity distribution, Kurt_{12} is 11.07, where $\mathrm{Kurt} = E(x-\mu)^4/\sigma^4$, where μ is the mean of the rainfall time-intensity distribution x, σ is the standard deviation of x, $E(t)$ is the expected value of the quantity t, and the subscript 12 denotes the time interval

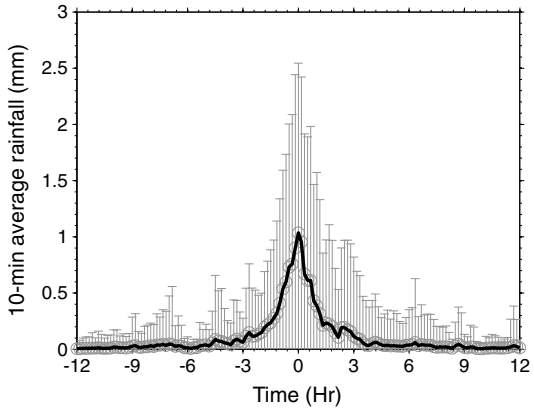

Figure 11. Time delay comparison of event occurrences with 10 min rainfall intensity average at the three nearest rain gauge stations. Each circle is the mean value for a 10 min interval and the associated error bar stands for the standard deviation. The relation is highlighted with a black line and shows that the event timing is for most coherent with rainfall intensity.

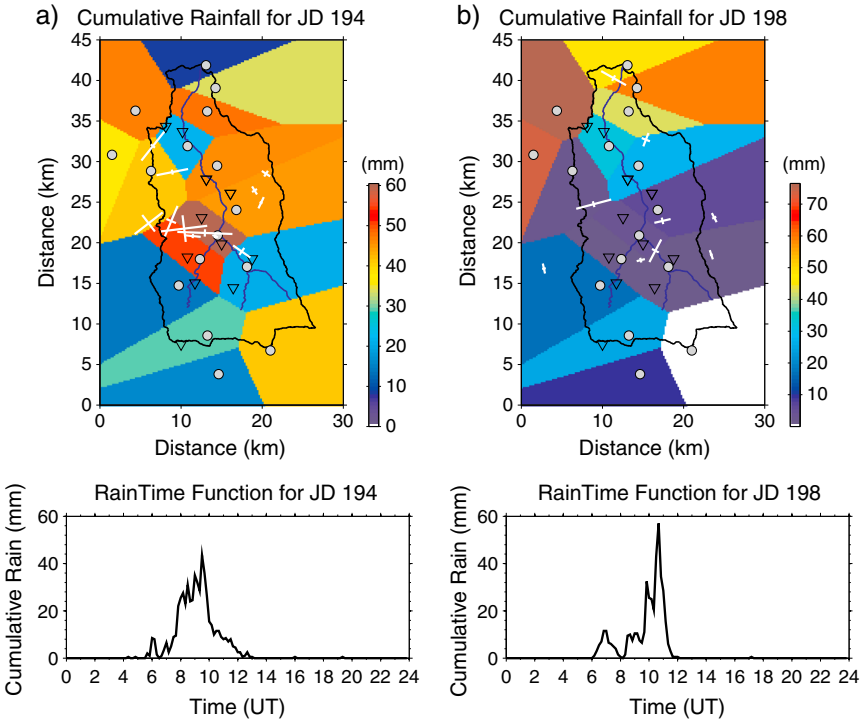

Figure 12. (top row) Comparison of the locations of seismologically detected and located geomorphic events (white bars represent the principal axes of the respective uncertainty ellipses) with the daily rainfall (shown in colors) recorded at 16 meteorological stations (gray dots) in and around the Chenyoulan catchment for Julian Days (a) 194 and (b) 198. Daily rainfall totals measured at a station are mapped in a Voronoi diagram, attributing the station value to all grid points nearest to that station. (bottom row) Rain time functions representing the 10 min sum of the time series recorded at the 16 meteorological stations on Days 194 and 198.

in hours. This very high kurtosis value reflects the marked peakness of the distribution, centered on the highest rainfall rates. For 3 and 2 h either side of an event, $\mathrm{Kurt}_3 = 3.13$ and $\mathrm{Kurt}_2 = 2.33$, respectively, indicating increased spread within these shorter time windows. This suggests that near-surface events could also be associated with high rainfall rates at other times during a rainstorm, but with a lesser likelihood. Importantly, the time-intensity distribution of rainfall relative to the recorded events was mildly positively skewed. Defining skewness, $\mathrm{Skew} = E(x-\mu)^3/\sigma^3$, where μ is the mean of the rainfall time-intensity distribution x, σ is the standard deviation of x, $E(t)$ is the expected value of the quantity t, and $\mathrm{Skew}_2 = 0.72$ and $\mathrm{Skew}_3 = 1.13$ for time windows of 2 and 3 h either side of an event, respectively. These small, positive values indicate that the rainfall preceding a recorded near-surface event did not prejudice the likelihood of that event. Instead, the recorded events were driven principally by instantaneous high rainfall rates, independent of prior rainfall.

[45] The frequency of detected near-surface events was positively correlated with 10 min catchment average rainfall (Figure 11). At rainfall rates below 1 mm in 10 min, the likelihood of occurrence of a detected event was about 1×10^{-3} per 10 min interval. For higher rainfall rates, the event likelihood increased exponentially, reaching about 1×10^{-2} per 10 min for rainfall rates around 6 mm in 10 min. The relation between rainfall rate and event likelihood has an exponential best fit, $F_{\mathrm{event}} = (e^{(0.37 \times P)})/1240$, where F_{event} is the frequency of seismically detected near-surface events per 10 min interval and P is the catchment-average 10 min rainfall rate ($R^2 = 0.88$).

[46] The significant simultaneity of convective rainfall and seismically recorded near-surface events and the systematic increase of event frequency with rainfall rate suggest that they are geomorphic in nature. Their short duration, coincidence with peak rainfall, and independence of antecedent precipitation match with hillslope processes that do not depend on the saturation state of underlying soil or regolith, such as rockfalls and minor rock avalanches, bank collapses, and debris slides. The rate with which these events occurred increased sharply with rainfall rate during the survey period in the Chenyoulan catchment. The nature of this relation between the rates of erosion and rainfall, though, is likely to be subject to spatial variation, even at the scale of the catchment. This is considered next.

[47] If rainfall is a principal driver of seismically recorded near-surface events in the Chenyoulan catchment, then there should also be a demonstrable link between the spatial patterns of rainfall intensity and event locations. This is indeed the case, but in a way that is complicated by other factors, as illustrated by the example of 2 days with similar, intense convective precipitation (Figure 12). Both days had up to about 60 mm of precipitation over a period of 4 h, but on Day 194, rainfall peaked in the center of the catchment, whereas it was most intense in the north on Day 198. Eleven seismically recorded events on Day 194 were located mainly in areas with the highest rainfall rate, suggesting that total daily rainfall was a control on their location. However 4

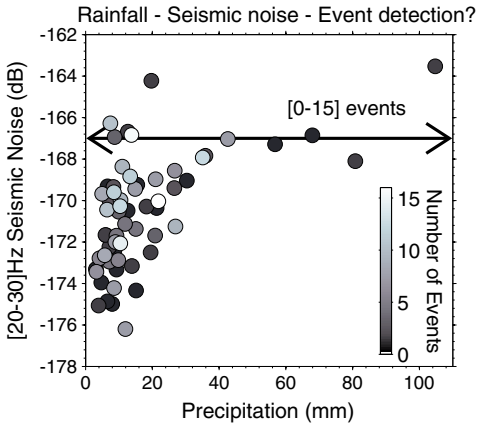

Figure 13. Influence of rainfall on the production of high-frequency seismic noise and the ability to seismologically detect geomorphic events. Each dot represents the average seismic energy recorded at 20–30 Hz during a rainstorm as a function of the cumulative precipitation during that rainstorm. Both quantities have been averaged over the available stations and the analysis was limited to rainstorms lasting more than 2 h. The gray tone of data points scales with the number of detected and located geomorphic events associated with the storm. The minimum level of seismic noise recorded for a given storm size is likely to reflect the rate of bed load transport in the main channels of the Chenyoulan catchment. Increase of river noise with increasing storm size may progressively mask the seismic signals of geomorphic events on hillslopes.

days later, nine seismically located events were dispersed across the catchment and away from areas with highest precipitation rates. Thus, instead of total daily rainfall, another aspect of the meteorological condition must have governed the location and timing of these events. One possibility is that recorded events were driven by short bursts of intense rainfall, which may have occurred away from locations with highest daily rainfall totals. Alternatively, elements of the topography of the Chenyoulan catchment may have been preconditioned for erosional events on a longer time scale. In this case, short intense rainfall in unstable topography may have played a role. On Day 198, the recorded near-surface activity coincided mostly with peak 10 min rainfall rates at the nearest station, strongly suggesting that they were triggered by brief but intense precipitation. However, the maximum recorded rainfall rates near locations of near-surface activity (1.5–4.0 mm/10 min) were not necessarily the highest rates recorded in the catchment during the storm of day 198 (20 mm/10 min). Four other examples, shown in the supporting information material (Figure S4), further illustrate this complexity. Hence, the sensitivity to rainfall drivers does not appear to have been uniform throughout the Chenyoulan catchment. A full analysis of this sensitivity is beyond the scope of this study.

5.2. Fluvial Masking of Hillslope Signals

[48] Rainfall-driven runoff of water in the catchment gives rise to enhanced stream flow and river sediment transport generating seismic noise. Due to overlap of the principal frequency bands of seismic signals from hillslope and river processes, river noise may limit the ability to seismically detect mass wasting events elsewhere, especially when the meteorological conditions favor hillslope activity. To explore this limitation, we have compared the number of detected near-surface events with the total precipitation and the average seismic noise level recorded at our stations for individual rainstorms lasting more than 2 h (Figure 13). This analysis was restricted to the 20–30 Hz frequency band, which can register signals from rapid mass wasting as well as fluvial bed load transport. For rainstorms with precipitation totals ranging from 3 to 105 mm, we have found a strong and systematic increase of the minimum seismic energy by ~12 dB, which corresponds to amplitudes 4 times higher on seismograms. We interpret this increase to reflect the rise in river noise with rising discharge and sediment transport. Above this minimum level, the recorded seismic energy varied by as much as 8 dB between storms with similar magnitude, over the limited precipitation range covered by our records. This may be due to varying levels of geomorphic activity on hillslopes in the area. Indeed, at lower precipitation totals, recorded seismic energy levels broadly correlated with the number of detected near-surface events, probably hillslope mass wasting. The paucity of larger storms during the monitoring interval precludes an evaluation of this apparent correlation at higher rainfall totals. However, if our interpretations are correct, then seismic energy from hillslope processes is added to the river signal, so that the general level of hillslope activity could be constrained if a relation between rainfall rate and river noise can be established independently. In mountain settings such as the Chenyoulan catchment, this relation is complicated by the fact that the river sediment load derives largely from adjacent hillslopes, causing variations in sediment concentrations by up to an order of magnitude for any given flood discharge [*Hovius et al*., 2000, *Dadson et al*., 2003], with attendant consequences for seismic energy levels. It is also clear that at elevated levels of river activity, the seismic signals of individual small hillslope events will become progressively masked, leaving only larger geomorphic events detectable. The global, negative relation between geomorphic event size and frequency [cf. *Hovius et al*., 1997; *Stark and Guzzetti*, 2009] may then cause a reduction of the number of detected events even though the rate of geomorphic activity can be assumed to increase with increased precipitation. At present, we do not have enough information to quantitatively explore these issues and their consequences for seismic detection of geomorphic process events.

6. Conclusions and Perspective

[49] Geomorphic processes have distinct seismic signals that can be registered by common seismometers. Therefore, it should be possible to monitor geomorphic activity in continuous mode and at the catchment scale with 2-D arrays of seismic instruments. This method has the potential to give a combination of spatial and temporal coverage and resolution that is not achievable through classic methods such as optical remote sensing and in situ observation. With an array of 14 seismometers and using a seismic detection approach and location technique based on the analysis of seismic amplitudes and their temporal features, we have detected and located 314 surface or near-surface events, with a mean accuracy of 1 km during the 2010 typhoon season in the 370 km^2, mountainous Chenyoulan catchment, central

Taiwan. The geomorphic nature of these events could not be confirmed from high-resolution satellite imagery and aerial photography, which did not show any geomorphic change over a monitoring interval of 100 days. However, their systematic association with specific meteorological conditions, which is unlikely for other potential sources at or near Earth's surface, underlines the plausibility of a geomorphic interpretation of these signals. In the absence of extreme and prolonged rainfall during the monitoring period, normally associated with passage of large typhoons, 69% of the detected events occurred during convective afternoon rainstorms with measured precipitation rates and totals of up to 18 mm/h and 43 mm, respectively. Within these rainstorms, detected events typically coincided with the highest recorded precipitation rate, irrespective of antecedent rainfall, suggesting that the triggered processes were driven by high instantaneous rainfall rates rather than cumulative precipitation. Moreover, the incidence rate of detected events increased exponentially with rainfall rate over the limited range of conditions during our study. The rainstorms during this period did not drive any large-scale landsliding, which dominated the catchment in the previous decade, and instead we tentatively attribute the recorded near-surface events to distributed, small-scale mass wasting and occasional debris flows. In contrast to the timing, the spatial pattern of seismically detected events did not systematically correlate with rainfall patterns. In some large rainstorms, most geomorphic activity coincided with the rainfall maximum, but not in others, highlighting the possible importance of site preconditioning, thresholds, and/or short-lived rainfall peaks, in addition to the physical characteristics of local slopes and substrates in setting the pattern and rate of erosion.

[50] On balance, it is highly unlikely that the recorded near-surface events were systematically associated with nongeomorphic sources. Instead, they probably represent the ensemble of significant erosional activity in the Chenyoulan catchment during the 100 day recording interval in 2010. Within uncertainty, the majority of the events (61%) were collocated with preexisting geomorphic structures (landslide scars, gullies). The likelihood of this association arising by accident in the Chenyoulan catchment is negligible. At sites of recent erosion, absence of vegetation precluded visual detection of renewed geomorphic activity. The seismically detected events then were most likely rockfalls, rock avalanches, minor landslides, and bank collapses at sites with prior activity within the past decade with additional activity on very steep slopes or under the cover of forest vegetation. However, we do not have an independent verification of this interpretation.

[51] Our results illustrate the potential and the challenges of seismic monitoring of geomorphic processes at the catchment scale. First, when fully proven, this approach will permit the detection and location of a range of geomorphic processes that occur throughout the landscape. Second, it could allow detection of events that remain invisible to extant remote-sensing techniques due to absence or opacity of vegetation, cloud cover or topographic overlay, and reactivation of existing erosion sites, thus complementing assessments of erosion based on optical remote sensing, which are prone to chronic underestimation of small events [cf. *Brardinoni and Church*, 2004]. And third, the approach could enable exploration of the relation between (meteorological) triggers and geomorphic response in temporal detail limited only by the frequency and density of the record of forcing and the spatial resolution of the seismic detection. The spatial resolution and sensitivity of seismic detection of near-surface events are limited by the location and distance between stations in a 2-D array. In our study, uncertainties on event location were 9% of the average distance between stations. It may be expected that reduction of this distance results in improved spatial resolution and location accuracy by enhancing the coherence of seismic signals between stations, but the precise nature of the trade-off between station distance and spatial resolution remains to be constrained. It should also be noted that seismic detection of individual near-surface events is hampered during rainstorms by elevated noise from turbulence and sediment transport in flooding rivers, making it essential to have a balance of stations located near and far from major river channels for monitoring of all geomorphic activity in a catchment.

[52] Further development of this approach must include a full analysis of detection limits, spatial resolution, and accuracy. Outstanding questions include the following: What is the relation between station spacing and spatial resolution? How accurate are seismically determined event locations when compared with independent, visual constraints? Can we constrain the source energy of a geomorphic event, or its magnitude, from recorded energy levels? What is the minimum event size that can reliably be detected? And what is the level of geomorphic activity such that the technique can no longer distinguish between individual geomorphic events? Farther down the line, it could be envisaged that this technique can be deployed for automated, real-time detection of geomorphic process events, such as rock avalanches, landslides, debris flows, and migrating bed load pulses, on the landscape scale. This would require isolation of the unique seismic characteristics of individual geomorphic processes, as well as efficient telemetry of seismic records, and could become a useful tool in natural hazard monitoring, early warning, and risk reduction. In the more immediate future, seismic monitoring of geomorphic processes at the landscape scale holds exciting potential for study of the minimum and necessary conditions for mass wasting, the relation between external forcing and geomorphic response, the transfer of eroded materials between process domains, and the relation between geomorphic activity and sedimentary product.

[53] **Acknowledgments.** This study was supported by the AXA Research Fund and the Isaac Newton Trust of the University of Cambridge. A.B. and N.H. are grateful to the Department of Geosciences of the National Taiwan University for providing the seismic instruments and generous logistic field support. We thank A. Densmore, H. Kao, V. Tsai, the Associate Editor, and an anonymous reviewer for their thorough and insistent comments and suggestions on earlier versions of the manuscript. The seismic data from the BATS (Broadband Array in Taiwan for Seismology) were provided by the IRIS Data Management Center.

References

Adams, P. N., C. D. Storlazzi, and R. S. Anderson (2005), Nearshore wave-induced cyclical flexing of sea cliffs, *J. Geophys. Res.*, *110*, F02002, doi:10.1029/2004JF000217.

Arattano, M., and L. Marchi (2005), Measurements of debris flow velocity through cross-correlation of instrumentation data, *Nat. Hazards Earth Syst. Sci.*, *5*, 137–142, doi:10.5194/nhess-5-137-2005.

Arattano, M., and L. Marchi (2008), Systems and sensors for debris-flow monitoring and warning, *Sensors*, *8*, 2436–2452, doi:10.3390/s8042436.

Badoux, A., C. Graf, J. Rhyner, R. Kuntner, and B. McArdell (2009), A debris-flow alarm system for the Alpine Illgraben catchment: Design and

performance, *Nat. Hazards*, *49*(3), 517–539, doi:10.1007/s11069-008-9303-x.

Barton, J., R. L. Slingerland, S. Pittman, and T. B. Gabrielson (2010), Monitoring coarse bedload transport with passive acoustic instrumentation: A field study, in *Bedload-Surrogate Monitoring Technologies: U.S. Geol. Surv. Scientific Investigations Report 2010-5091*, edited by J. R. Gray, J. B. Laronne, and J. D. G. Marr, U.S. Geological Survey, Reston, Virginia.

Berti, M., R. Genevois, R. LaHusen, A. Simoni, and P. R. Tecca (2000), Debris flow monitoring in the acquabona watershed on the Dolomites (Italian alps, *Phys. Chem. Earth Part B*, *25*(9), 707–715, doi:10.1016/S1464-1909(00)00090-3.

Bollinger, L., F. Perrier, J.-P. Avouac, S. Sapkota, U. Gautam, and D. R. Tiwari (2007), Seasonal modulation of seismicity in the Himalaya of Nepal, *Geophys. Res. Lett.*, *34*, L08304, doi:10.1029/2006GL029192.

Brardinoni, F., and M. Church (2004), Representing the landslide magnitude-frequency relation: Capilano River basin, British Columbia, *Earth Surf. Process. Landforms*, *29*, 115–124, doi:10.1002/esp.1029.

Brardinoni, F., O. Slaymaker, and M. A. Hassan (2003), Landslide inventory in a rugged forested watershed: A comparison between air-photo and field survey data, *Geomorphology*, *54*(3-4), 179–196, doi:10.1016/S0169-555X(02)00355-0.

Brodsky, E. E., E. Gordeev, and H. Kanamori (2003), Landslide basal friction as measured by seismic waves, *Geophys. Res. Lett.*, *30*(24), 2236, doi:10.1029/2003GL018485.

Burtin, A., L. Bollinger, J. Vergne, R. Cattin, and J. L. Nábělek (2008), Spectral analysis of seismic noise induced by rivers: A new tool to monitor spatiotemporal changes in stream hydrodynamics, *J. Geophys. Res.*, *113*, B05301, doi:10.1029/2007JB005034.

Burtin, A., L. Bollinger, R. Cattin, J. Vergne, and J. L. Nábělek (2009), Spatiotemporal sequence of Himalayan debris flow from analysis of high-frequency seismic noise, *J. Geophys. Res.*, *114*, F04009, doi:10.1029/2008JF001198.

Burtin, A., J. Vergne, L. Rivera, and P. Dubernet (2010), Location of river-induced seismic signal from noise correlation functions, *Geophys. J. Int.*, *182*, 1161–1173, doi:10.1111/j.1365-246X.2010.04701.x.

Burtin, A., R. Cattin, L. Bollinger, J. Vergne, P. Steer, A. Robert, N. Findling , and C. Tiberi (2011), Towards the hydrologic and bed load monitoring from high-frequency seismic noise in a braided river: the "torrent de St Pierre", French Alps, *J. Hydrol.*, doi:10.1016/j.jhydrol.2011.07.014.

Chang, L.-W., P.-F. Hsieh, and C.-W. Lin (2006), Landslide identification based on FORMOSAT-2 multispectral imagery by wavelet-based texture feature extraction, *Geoscience and Remote Sensing Symposium*. IGARSS 2006. IEEE International Conference, 3317–3320, doi:10.1109/IGARSS.2006.852.

Chen, C.-S., and Y.-L. Chen (2003), The rainfall characteristics of Taiwan, *Mon. Weather Rev.*, *131*, 1323–1341, doi:10.1175/1520-0493(2003)131<1323:TRCOT>2.0.CO;2.

Chien, F.-C., and H.-C. Kuo (2011), On the extreme rainfall of Typhoon Morakot (2009), *J. Geophys. Res.*, *116*, D05104, doi:10.1029/2010JD015092.

Clarke, B. A., and D. W. Burbank (2011), Quantifying bedrock-fracture patterns within the shallow subsurface: Implications for rock mass strength, bedrock landslides, and erodibility, *J. Geophys. Res.*, *116*, F04009, doi:10.1029/2011JF001987.

Dadson, S. J., et al. (2003), Links between erosion, runoff variability and seismicity in the Taiwan orogen, *Nature*, *426*, 648–651, doi:10.1038/nature02150.

Dadson, S. J., et al. (2004), Earthquake-triggered increase in sediment delivery from an active mountain belt, *Geology*, *32*, 733–736, doi:10.1130/G20639.1.

Dammeier, F., J. R. Moore, F. Haslinger, and S. Loew (2011), Characterization of alpine rockslides using statistical analysis of seismic signals, *J. Geophys. Res.*, *116*, F04024, doi:10.1029/2011JF002037.

Deparis, J., D. Jongmans, F. Cotton, L. Baillet, F. Thouvenot, and D. Hantz (2008), Analysis of rock-fall and rock-fall avalanche seismograms in the French alps, *Bull. Seismol. Soc. Am.*, *98*(4), 1781–1796, doi:10.1785/0120070082.

Ekström, G., and C. P. Stark (2013), Simple scaling of catastrophic landslide dynamics, *Science*, *339*(6126), 1416–1419, doi:10.1126/science.1232887.

Favreau, P., A. Mangeney, A. Lucas, G. Crosta, and F. Bouchut (2010), Numerical modeling of landquakes, *Geophys. Res. Lett.*, *37*, L15305, doi:10.1029/2010GL043512.

Galewsky, J., C. P. Stark, S. Dadson, C.-C. Wu, A. H. Sobel, and M.-J. Horng (2006), Tropical cyclone triggering of sediment discharge in Taiwan, *J. Geophys. Res.*, *111*, F03014, doi:10.1029/2005JF000428.

Guzzetti, F., M. Cardinali, P. Reichenbach, and A. Carrara (2000), Comparing landslide maps: A case study in the upper Tiber River basin, central Italy, *Environ. Manage.*, *25*(3), 247–263, doi:10.1007/s002679910020.

Havskov, J., and G. Alguacil (2006), Instrumentation in earthquake seismology, *Modern Approaches in Geophysics*, 22, 360 pp., Springer, Dordrecht, The Netherlands.

Helmstetter, A., and S. Garambois (2010), Seismic monitoring of Séchilienne rockslide (French Alps): Analysis of seismic signals and their correlation with rainfalls, *J. Geophys. Res.*, *115*, F03016, doi:10.1029/2009JF001532.

Hibert, C., A. Mangeney, G. Grandjean, and N. M. Shapiro (2011), Slope instabilities in Dolomieu crater, Réunion Island: From seismic signals to rockfall characteristics, *J. Geophys. Res.*, *116*, F04032, doi:10.1029/2011JF002038.

Hovius, N., C. P. Stark, and P. A. Allen (1997), Sediment flux from a mountain belt derived by landslide mapping, *Geology*, *25*, 231–234, doi:10.1130/0091-7613(1997)025<0231:SFFAMB>2.3.CO;2.

Hovius, N., C. P. Stark, C.-H. Tsu, and L.-J. Chuan (2000), Supply and removal of sediment in a landslide dominated mountain belt: Central Range, Taiwan, *The Journal of Geology*, *108*(1), 73–89, doi:10.1086/314387.

Hovius, N., P. Meunier, C.-W. Lin, H. Chen, Y.-G. Chen, S. Dadson, M.-J. Horng, and M. Lines (2011), Prolonged seismically induced erosion and the mass balance of a large earthquake, *Earth Planet. Sci. Lett.*, *304*(3-4), 347–355, doi:10.1016/j.epsl.2011.02.005.

Hsiao, T., B. Lee, T. Chou, H. Lien, and Y. Chang (2007), Debris flow monitoring system and observed event in Taiwan: A case study at Aiyuzi River, *Wuhan University Journal of Natural Sciences*, *12*(4), 610–618, doi:10.1007/s11859-006-0298-4.

Hsu, L., N. J. Finnegan, and E. E. Brodsky (2011), A seismic signature of river bedload transport during storm events, *Geophys. Res. Lett.*, *38*, L13407, doi:10.1029/2011GL047759.

Huang, C.-J., H.-Y. Yin, C.-Y. Chen, C.-H. Yeh, and C.-L. Wang (2007), Ground vibrations produced by rock motions and debris flows, *J. Geophys. Res.*, *112*, F02014, doi:10.1029/2005JF000437.

Itakura, Y., H. Inaba, and T. Sawada (2005), A debris-flow monitoring devices and methods bibliography, *Nat. Hazards Earth Syst. Sci.*, *5*(6), 971–977, doi:10.5194/nhess-5-971-2005.

Kanamori, H., and J. W. Given (1982), Analysis of long-period seismic waves excited by the May 18, 1980, eruption of Mount St. Helens—A terrestrial monopole?, *J. Geophys. Res.*, *87*(B7), 5422–5432, doi:10.1029/JB087iB07p05422.

Kao, H., and W.-P. Chen (2000), The Chi-Chi earthquake sequence: Active, out-of-sequence thrust faulting in Taiwan, *Science*, *288*(5475), 2346–2349, doi:10.1126/science.288.5475.2346.

Kao, H., and S.-J. Shan (2004), The source-scanning algorithm: Mapping the distribution of seismic sources in time and space, *Geophysical Journal International*, *157*, 589–594, doi:10.1111/j.1365-246X.2004.02276.x.

Kao, H., S.-J. Shan, H. Dragert, G. Rogers, J. F. Cassidy, K. Wang, T. S. James, and K. Ramachandran (2006), Spatial temporal patterns of seismic tremors in northern Cascadia, *J. Geophys. Res.*, *111*, B03309, doi:10.1029/2005JB003727.

Kao, H., C.-W. Kan, R.-Y. Chen, C.-H. Chang, A. Rosenberger, T.-C. Shin, P.-L. Leu, K.-W. Kuo, and W.-T. Liang (2012), Locating, monitoring, and characterizing typhoon-induced landslides with real-time seismic signals, *Landslides*, *1-7*, doi:10.1007/s10346-012-0322-z.

Kappus, M. E., and F. L. Vernon (1991), Acoustic signature of thunder from seismic records, *J. Geophys. Res.*, *96*(D6), 10,989–11,006, doi:10.1029/91JD00789.

La Rocca, M., D. Galluzzo, G. Saccorotti, S. Tinti, G. B. Cimini, and E. Del Pezzo (2004), Seismic signals associated with landslides and with a tsunami at Stromboli Volcano, Italy, *Bull. Seismol. Soc. Am.*, *94*(5), 1850–1867, doi:10.1785/012003238.

Lacroix, P., and A. Helmstetter (2011), Location of seismic signals associated with microearthquakes and rockfalls on the Séchilienne landslide, French alps, *Bull. Seismol. Soc. Am.*, *101*(1), 341–353, doi:10.1785/0120100110.

Lacroix, P., J.-R. Grasso, J. Roulle, G. Giraud, D. Goetz, S. Morin, and A. Helmstetter (2012), Monitoring of snow avalanches using a seismic array: Location, speed estimation, and relationships to meteorological variables, *J. Geophys. Res.*, *117*, F01034, doi:10.1029/2011JF002106.

Lay, T., and T. C. Wallace (1995), *Modern Global Seismology*, Academic Press, 521 pp., San Diego, Calif.

Lee, C. T., and B. R. Tsai (2008), Mapping Vs30 in Taiwan, *Terr. Atmos. Ocean. Sci.*, *19*, 671–682, doi:10.3319/TAO.2008.19.6.671(PT).

Leprettre, B., J.-P. Navarre, J.-M. Panel, F. Touvier, A. Taillefer, and J. Roulle (1998), Prototype for operational seismic detection of natural avalanches, *Ann. Glaciol.*, *26*, 313–318.

Lin, G.-W., H. Chen, N. Hovius, M.-J. Horng, S. Dadson, P. Meunier, and M. Lines (2008), Effects of earthquake and cyclone sequencing on landsliding and fluvial sediment transfer in a mountain catchment, *Earth Surf. Processes Landforms*, *33*, 1354–1373, doi:10.1002/esp.1716.

Lin, C. H., H. Kumagai, M. Ando, and T. C. Shin (2010), Detection of landslides and submarine slumps using broadband seismic networks, *Geophys. Res. Lett.*, *37*, L22309, doi:10.1029/2010GL044685.

Lin, C.-W., W.-S. Chang, S.-H. Liu, T.-T. Tsai, S.-P. Lee, Y.-C. Tsang, C.-L. Shieh, and C.-M. Tseng (2011), Landslides triggered by the 7 August 2009 Typhoon Morakot in southern Taiwan, *Eng. Geol.*, *123*(1-2), 3–12, doi:10.1016/j.enggeo.2011.06.007.

Marchi, L., M. Arattano, and A. M. Deganutti (2002), Ten years of debris-flow monitoring in the Moscardo Torrent (Italian Alps), *Geomorphology*, *46*(1-2), 1–17, doi:10.1016/S0169-555X(01)00162-3.

McNamara, D. E., and R. P. Buland (2004), Ambient noise levels in the continental United States, *Bull. Seismol. Soc. Am.*, *94*(4), 1517–1527, doi:10.1785/012003001.

Meunier, P., N. Hovius, and A. J. Haines (2007), Regional patterns of earthquake-triggered landslides and their relation to ground motion, *Geophys. Res. Lett.*, *34*, L20408, doi:10.1029/2007GL031337.

Nábělek, J., G. Hetényi, J. Vergne, S. Sapkota, B. Kafle, M. Jiang, H. Su, J. Chen, B.-S. Huang, and the Hi-CLIMB Team (2009), Underplating in the Himalaya-Tibet collision zone revealed by the Hi-CLIMB experiment, *Science*, *325*, 1371–1374, doi:10.1126/science.1167719.

O'Connell-Rodwell, C. E., L. A. Hart, and B. T. Arnason (2011), Exploring the potential use of seismic waves as a communication channel by elephants and other large mammals, *Amer. Zool.*, *41*(5), 1157–1170, doi:10.1093/icb/41.5.1157.

Reid, L. M. (1998), Calculation of average landslide frequency using climatic records, *Water Resour. Res.*, *34*(4), 869–877, doi:10.1029/97WR02682.

Scarpetta, S., F. Giudicepietro, E. C. Ezin, S. Petrosino, E. Del Pezzo, M. Martini, and M. Marinaro (2005), Automatic classification of seismic signals at Mt. Vesuvius volcano, Italy, using neural networks, *Bull. Seismol. Soc. Am.*, *95*(1), 185–196, doi:10.1785/0120030075.

Sella, G. F., T. H. Dixon, and A. Mao (2002), REVEL: A model for recent plate velocities from space geodesy, *J. Geophys. Res.*, *107*, 2081, doi:10.1029/2000JB000033.

Sibuet, J.-C., and S.-K. Hsu (2004), How was Taiwan created?, *Tectonophysics*, *379*(1-4), 159–181, doi:10.1016/j.tecto.2003.10.022.

St. Lawrence, W., and T. R. Williams (1976), Seismic signals associated with avalanches, *J. Glaciol.*, *17*(77), 521–526.

Stark, C. P., and F. Guzzetti (2009), Landslide rupture and the probability distribution of mobilized debris volumes, *J. Geophys. Res.*, *114*, F00A02, doi:10.1029/2008JF001008.

Stark, C. P., J. R. Barbour, Y. S. Hayakawa, T. Hattanji, N. Hovius, H. Chen, C.-W. Lin, M.-J. Horng, K.-Q. Xu, and Y. Fukahata (2010), The climatic signature of incised river meanders, *Science*, *327*(5972), 1497–1501, doi:10.1126/science.1184406.

Streig, A. R., C. M. Rubin, W.-S. Chen, Y.-G. Chen, L.-S. Lee, S. C. Thompson, C. Madden, and S.-T. Lu (2007), Evidence for prehistoric coseismic folding along the Tsaotun segment of the Chelungpu fault near Nan-Tou, Taiwan, *J. Geophys. Res.*, *112*, B03S06, doi:10.1029/2006JB004493.

Suriñach, E., I. Vilajosana, G. Khazaradze, B. Biescas, G. Furdada, and J. M. Vilaplana (2005), Seismic detection and characterization of landslides and other mass movements, *Nat. Hazards Earth Syst. Sci.*, *5*, 791–798, doi:10.5194/nhess-5-791-2005.

Swanson, P. L. (1992), Mining-induced seismicity in faulted geologic structures: An analysis of seismicity-induced slip potential, *Pure Appl. Geophys.*, *139*(3), 657–676, doi:10.1007/BF00879957.

Toksöz, M. N., and D. H. Johnson (1981), *Seismic Wave Attenuation*, edited by M. N. Toksöz and D. H. Johnson, Society of Exploration Geophysicists, Tulsa, OK.

Tsai, V. C., B. Minchew, M. P. Lamb, and J.-P. Ampuero (2012), A physical model for seismic noise generation from sediment transport in rivers, *Geophys. Res. Lett.*, *39*, L02404, doi:10.1029/2011GL050255.

Turowski, J. M., E. M. Yager, A. Badoux, D. Rickenmann, and P. Molnar (2009), The impact of exceptional events on erosion, bedload transport and channel stability in a step-pool channel, *Earth Surf. Process. Landforms*, *34*, 1661–1673, doi:10.1002/esp.1855.

Vilajosana, I., E. Suriñach, A. Abellán, G. Khazaradze, D. Garcia, and J. Llosa (2008), Rockfall induced seismic signals: Case study in Montserrat, Catalonia, *Nat. Hazards Earth Syst. Sci.*, *8*, 805–812, doi:10.5194/nhess-8-805-2008.

Wdowinski, S., and I. Tsukanov (2011), Disaster triggers disaster: Earthquake triggering by tropical cyclones, Abstract U53E-06 presented at 2011 Fall Meeting, AGU, San Francisco, Calif., 5-9 Dec.

Withers, M. M., R. C. Aster, C. J. Young, and E. P. Chael (1996), High frequency analysis of seismic background noise as a function of wind speed and shallow depth, *Bull. Seismol. Soc. Am.*, *86*(5), 1507–1515.